Thin Solid Films 806 (2024) 140527

Contents lists available at ScienceDirect

Thin Solid Films

journal homepage: www.elsevier.com/locate/tsf

Characterization of MoS_2:Nb sputtered thin films. An application as hole transport layer in Cu_2ZnSnS_4/Si tandem solar cells

Claudia Malerba *, Matteo Valentini, Francesca Menchini, Daniele Mirabile Gattia, Enrico Salza, Alberto Mittiga

ENEA, Casaccia Research Center, via Anguillarese 301, 00123 Rome, Italy

ARTICLE INFO

Keywords:
Molybdenum disulfide
Sputtering
Hole transport layer
Tandem solar cells
Kesterite
Copper zinc tin sulfide
Silicon
Intermediate contact
Selective contacts

ABSTRACT

MoS_2:Nb films deposited by radio-frequency magnetron sputtering are investigated in view of their application in infrared (IR)-transparent contacts for tandem photovoltaic devices.

This material is already known to give a good electrical contact with p-type chalcogenide semiconductors, which are typically grown onto opaque molybdenum metallic contacts and a MoS_2 layer spontaneously forms at the back interface during the on-top semiconductor growth. Our study explores a different approach, which involves the direct growth of IR-transparent MoS_2:Nb films via sputtering inside complete photovoltaic devices, like Cu_2ZnSnS_4 (CZTS)-based single junction solar cells and CZTS/Si tandem devices. Films deposited at different sputtering pressures are compared by analysing their microstructure, morphology, chemical composition, optical and electrical properties. The effects of post-deposition sulfurization treatments are also investigated. We find that MoS_2:Nb films deposited at around 0.1 Pa exhibit compactness but show a notable sulfur deficit ([S]/[Mo]≈ 1.4), a significant sub-bandgap optical absorptance and lack of crystallinity. Increasing the Ar pressure to 1 Pa raises the [S]/[Mo] ratio to 2.2, yielding crystalline films with good IR-transparency, although with a porous morphology. Despite 0.5 wt% Nb-doping of the sputtering target, the as-deposited films demonstrate n-type conductivity likely due to uncontrolled impurities and intrinsic defects. Ultraviolet Photoemission Spectroscopy measurements suggest that films' work function higher than 5 eV can be obtained with a post-deposition sulfurization, making these materials suitable as Hole Transport Layer in photovoltaic applications. A similar increase in work function is expected in the CZTS/MoS_2 junctions, since the sputtered MoS_2:Nb films undergo a sulfurization process needed to obtain the overlying polycrystalline CZTS absorber.

CZTS solar cells produced with sputtered MoS_2 and Transparent Conductive Oxides contacts on glass substrates, despite plagued by severe adhesion problems, show the potentiality to give efficiencies comparable to reference devices with standard Mo back contact. Fabrication of CZTS/Si tandem devices on textured silicon bottom cells yields a maximum efficiency of 4.4 %, primarily hindered by the low quality of the CZTS film on textured substrates. Nonetheless, optoelectronic characterizations based on both spectrophotometric and quantum efficiency measurements confirm a good IR transparency of the MoS_2-based intermediate contacts and the desired electrical behaviour.

1. Introduction

The development of several kinds of emerging tandem photovoltaic (PV) devices would greatly benefit from the availability of an infrared (IR) transparent hole transport layer (HTL) with a high work function. Low cost, high stability and ease of deposition over a large area would also be attractive requirements. In this work the use of sputtered MoS_2 as hole transport layer is proposed and evaluated, as several properties of the material make it a good candidate. MoS_2 has an indirect optical gap of 1.17–1.23 eV [1,2] while the first direct gap is at 1.85 eV [3]. The indirect gap gives a rather weak absorption so that films with a thickness of a few tens of nanometers are quite transparent for wavelengths greater than 800 nm. MoS_2 photothreshold (i.e. the energy difference between the vacuum level and the valence band maximum) is quite high being about 5.6 eV [4]. It follows that if p-type doped MoS_2 could be obtained it would show a work function larger than 5 eV. However,

* Corresponding author.
E-mail address: claudia.malerba@enea.it (C. Malerba).

https://doi.org/10.1016/j.tsf.2024.140527
Received 18 April 2024; Received in revised form 5 September 2024; Accepted 6 September 2024
Available online 7 September 2024

MoS_2 shows a native propensity toward n-type conductivity, which is often imputed to sulphur vacancies [5–7] (even though their role as donors is still controversial [8]), as well as to uncontrolled impurities [9–11]. It would be therefore advantageous to dope MoS_2 with a suitable acceptor impurity [12–15] and, according to the literature, Niobium is a good choice [16,17].

Non-intentionally doped MoS_2 was already employed in a monolithic Cu_2ZnSnS_4 (CZTS)/Si tandem device where a MoS_2/FTO/ZnO multilayer structure was used as intermediate contact [18] between the top and the bottom cells. The MoS_2 layer used in this stack was obtained by metallic Mo sulfurization, but this technique is not optimal since an incomplete Mo sulfurization can take place if a too mild process is used, while a Transparent Conductive Oxides (TCO) degradation can occur if a too aggressive process is used.

In this work, a process route which involves a direct radio frequency (RF) sputtering deposition of MoS_2:Nb is investigated using a target with a MoS_2/NbS_2=99.5/0.5 wt% composition. This approach allows a better control of thickness and transparency of the MoS_2:Nb layer and preserves the underlying TCOs from degradation. In addition, Niobium doping should be able to shift the material conductivity towards p-type, improving hole transport at the CZTS/MoS_2:Nb interface. The Niobium concentration in the target is chosen following a paper by Suh et al. [16] where it is reported that doping a single crystal of MoS_2 with 0.5 % Nb is enough to produce a degenerate p-type doped material with a hole concentration of 3×10^{19} cm^{-3}. The correlation between sputtering conditions and MoS_2:Nb film properties is investigated by analysing the films microstructure, morphology, chemical composition, optical and electrical properties. The influence of post deposition annealing treatments in a sulfur atmosphere (sulfurization) is also investigated. The study of sulfurized MoS_2:Nb films is interesting also in view of their possible applications in CZTS solar cells, since a sulfurization treatment is a typical step of the absorber growth process and therefore the MoS_2:Nb layer, if used as back contact, will indirectly undergo a similar treatment. For this reason, sulfurization conditions similar to those typically used for the absorber are chosen for this study. Finally, the properties of sputtered MoS_2:Nb films as IR-transparent HTLs are investigated by producing complete PV devices, like CZTS single junction solar cells and textured CZTS/Si tandem devices.

2. Experimental section

2.1. MoS_2:Nb growth and characterization

MoS_2:Nb films were deposited with a Kenosistec magnetron RF sputtering system using a 0.5 wt% Nb-doped MoS_2 target of 150 cm^2 area and 0.6 cm thick, purchased from Process Materials Inc. (target-to-substrate distance about 10 cm), with a constant RF power of 150 W (power density 1 W/cm^2), varying the Ar working pressure between 0.11 and 1 Pa. The substrate temperature was set to 180 °C (to align with the optimized conditions of TCOs deposition, details provided below), but some experiments were also conducted at room temperature for comparison. The film thickness ranged from 30 to 200 nm.

In all the deposition runs at least one 2.5×7.5 cm^2 Corning Eagle XG borosilicate glass (BSG) was inserted, to be used for the microstructural, chemical and optoelectronic characterization of the bare MoS_2:Nb films. The borosilicate glass was preferred to the standard soda-lime glass to avoid sodium contamination since it is well known that Na^+ ions can easily intercalate in between the MoS_2:Nb layers behaving as donors [19,20].

A Field-Emission Gun Scanning Electron Microscope (FEG-SEM LEO 35, Zeiss) equipped with an Oxford EDX detector for Energy Dispersive X-ray Spectroscopy (EDX) was used for morphological and chemical characterization of the materials. The SEM images were collected using an In-Lens type-I secondary electron (SE1) detector, with an electron beam energy of 3 keV and a working distance (WD) of 3 mm. For the EDX spectra, a 20 keV electron beam energy and a WD of 8.5 mm were utilized. The film cross-sections were prepared for SEM analysis by scribing the backside of the substrate and fracturing the sample, ensuring that the film cross-section intended for observation remained undamaged. These samples, along with those used for the planar-view analysis, were then directly mounted on the stubs for the SEM analysis, without any additional polishing or coating deposition. For each sample, several regions (with area varying between 200 and 2000 μm^2) were analysed changing the magnification settings and two representative images (in cross-sectional and planar view) were chosen and reported in this work.

X-Ray Diffraction (XRD) measurements were performed with a SmartLab Rigaku, with Cukα source radiation and a monochromator in the diffracted beam. The diffractometer was operated at 40 kV and 30 mA. XRD patterns were acquired in the 2theta range from 5 to 90° with a step size of 0.025 and a time per step of 5–10 s. Different types of measurements were performed in Bragg/Brentano standard configuration and with the X-Ray source fixed at low incidence angles.

X-ray photoelectron spectroscopy (XPS) measurements were carried out in a Vacuum Generator ESCA LAB MKII system, using the Al Kα line as an x-ray source. Ultraviolet Photoelectron Spectroscopy (UPS) measurements were performed in the same system, employing the He I line radiation for the excitation of photoelectron emission. A bias voltage was applied to the samples to appreciate the secondary electrons cut-off. The kinetic energy scale of the spectra was calibrated to the Fermi Energy position of an Au reference.

A depth profiling analysis of the samples was performed by Glow Discharge Optical Emission Spectroscopy (GDOES) measurements using a Horiba Jobin Yvon GD Profiler 2 spectrometer with an anode diameter of 4 mm.

Spectrophotometric measurements were made with a Perkin-Elmer LAMBDA 950 system equipped with a 150 mm integrating sphere to investigate the materials optical properties in the range from 250 to 2500 nm.

Weight and geometry measurements were performed to estimate the material density and porosity. The film weight was obtained as difference between that of the total sample and of the bare substrate, measured before deposition. 10 μm-thick Al foils were used as lightweight substrates for these measurements in order to improve the accuracy of the results. As a further verification, the initial substrate weight was measured again after the film deposition, removing the MoS_2:Nb layer in H_2O_2. The thickness and area of each film were obtained using profilometer, calipers, microscope images and SEM cross sections. It must be noted that a small uncertainty in the sample thickness (due to measurement error or sample inhomogeneity) leads to a certain error in the final density evaluation, which can be determined within a reasonable error of ± 0.2 g/cm^{-3}. Due to the uncertainty associated to the measured density, the calculated porosity of the samples is reasonably affected by an absolute error of about 5÷10 %. However, the porosity values are confirmed by the optical simulations results obtained by the software KSEMAWc [21], as detailed in the Appendix A.

Electrical resistivity was obtained by 4-probe measurements on MoS_2:Nb /glass samples with a Napson RT-7 system or (in the case of samples with sheet resistance > 300 KΩ/square) derived from current-voltage measurements made in planar configuration, with gold contacts evaporated onto the MoS_2:Nb film surface, using a Keithley i236 instrument. The electrical behavior of MoS_2:Nb films was also indirectly investigated by measuring the current density-voltage (J-V) curves of MoS_2:Nb /c-Si heterojunctions, produced using both n-type and p-type Si wafer. For this purpose, in some deposition runs two silicon wafers (p-type and n-type) were also inserted. The wafers were deoxidized in a chemical bath of 1 % HF in DIW before the deposition. The electrical contact on the top MoS_2:Nb layer was made by gold dot evaporation while the back ohmic contact on c-Si wafer was made using an In-Ga eutectic.

2.2. Deposition of MoS_2:Nb/TCOs contacts for CZTS solar cells and CZTS/Si tandem devices

Sputtered MoS_2:Nb films were tested as back contact in CZTS photovoltaic devices and as intermediate contact in CZTS/Si tandem solar cells. To obtain a conductive and semi-transparent contact, MoS_2:Nb/FTO/IWO trilayer structures were produced. Tungsten-doped Indium Oxide (IWO) was used to get a reasonable sheet resistance (<20 Ω/square) while Fluorine-doped Tin Oxide (FTO) was introduced to protect the IWO from the reactive atmosphere present during the CZTS sulfurization thanks to its good chemical stability. The MoS_2:Nb/FTO/IWO trilayer was deposited inside the same sputtering system, without breaking the vacuum, keeping the substrate at about 180 °C. The sputtering conditions of the TCOs (IWO and FTO) were previously optimized to obtain films with a good transparency, a sufficiently high conductivity and a good chemical stability. The IWO layer (about 300 nm thick) was RF-sputtered from an IWO target (In_2O_3/WO_3 = 99/1 wt%) at 300 W power, a sputtering pressure of 0.5 Pa and with the following gas fluxes: Ar = 38.4 sccm, H_2 = 1.6 sccm, O_2 = 0.5 sccm. The FTO layer (about 350 nm thick) was deposited by DC-sputtering from an FTO target (SnO_2/SnF_2 = 97/3 wt%) at 300 W at an Ar sputtering pressure of 0.8 Pa with additional oxygen flow of 2 sccm (Ar/O_2 flow ratio 60/2). MoS_2:Nb films were then deposited onto the FTO using different sputtering conditions explored in this work.

The CZTS absorber was grown using a two-step process already detailed in the literature [22]: i) co-sputtering deposition of a 900 nm thick quaternary precursor layer from three targets of Cu, ZnS and SnS; ii) thermal treatment at 580 °C for 1 hour in sulfur atmosphere (sulfurization), necessary to introduce the correct amount of sulfur into the absorber and to promote the grain growth. The sputtering powers applied to each target were properly settled to keep the precursors composition close to the well-known optimum range for photovoltaic applications ([Cu]/[Zn+Sn]≈0.75 and [Zn]/[Sn]≈1.2) ([23,24]). A 7 nm thick NaF layer was evaporated as sodium source on the precursor surface before the sulfurization treatment; Na doping is indeed known to promote the CZTS grain growth and to play a beneficial role in defect passivation [25]. The devices were then completed with the deposition of a CdS buffer layer by chemical bath and with a sputtered ZnO/IWO front contact.

CdS buffer layer (about 60 nm) was deposited by chemical bath at about 60 °C in a 200 ml aqueous solution of NH_4OH (Sigma-Aldrich 28 %) (M(NH_3) = 1.8 M), $CdSO_4$ 1.5 mM and thiourea (1.09 g in 200 ml, M (CH_4N_2S) = 71.6 mM). CdS film reaches a thickness of about 60 nm in 9 min, after which sample is removed from the bath and washed in deionized water. TCOs layers were deposited by RF magnetron-sputtering (in the same Kenosistec system used for MoS_2:Nb) at about 180 °C substrate temperature using the following conditions: (i) ZnO: RF-Power density = 1.33 W/cm^2, Ar working pressure 0.5 Pa, thickness 40 nm; ii) IWO: RF-Power density = 2 W/cm^2, target composition In_2O_3/WO_3 (99/1 wt%), Ar working pressure 0.5 Pa (fluxes: Ar = 38.4 sccm, H_2 = 1.6 sccm, O_2 = 0.5 sccm), thickness 250 nm.

The scheme of these fabrication process steps is reported in Fig. 1. IWO/FTO/MoS_2:Nb/CZTS/CdS/IWO/ZnO structures were deposited both on borosilicate glass for characterization of the semitransparent CZTS cells and on textured Si bottom cells for tandem devices. Details about silicon bottom cell fabrication are reported in our previous work [18].

The devices were characterized by External Quantum Efficiency (EQE) measurements and current density-voltage measurements under AM1.5 light conditions using a WACOM WXS 140S-10 class A solar simulator.

3. Results and discussion

3.1. As-deposited MoS_2:Nb thin films: effect of the sputtering pressure

Table 1 reports a list of MoS_2:Nb samples produced by sputtering deposition at three different Ar working pressures, ranging between 0.11 and 1 Pa. The deposition time was set to obtain sufficiently thick samples (nominal thickness around 200 nm), suitable for chemical, electrical and spectrophotometric characterization. The film properties and process conditions are reported in Table 1. The sample properties (such as the chemical composition, electrical resistivity, morphology and optical behaviour) were found to be strongly dependent on the sputtering pressure, as explained in the following.

The chemical composition of as-deposited (as-dep) films derived from EDX measurements is shown in Fig. 2a, reporting the [S]/[Mo] ratio as a function of the sputtering pressure. The large error on EDX data may suggest a certain composition inhomogeneity but could also derive form the measurement error due to the partial superposition of the L_{α}–Mo and K_{α}-S EDX signals. Despite the uncertainty in the compositional results, measurements repeated on different samples grown in the same conditions reveal a clear increasing trend of the sulfur incorporation as the sputtering pressure increases: [S]/[Mo] values much lower than 2 are indeed found for the lowest pressure (0.11 Pa) whereas more stoichiometric samples, with [S]/[Mo] close or slightly larger than 2, are obtained for deposition at 1 Pa. These results are also in accordance with XPS measurements which confirmed the presence of metallic Mo in samples deposited at pressures lower than 1 Pa (a comparison between as-dep films produced at 0.5 and 1 Pa is shown in Fig. B1).

For decreasing sputtering pressure, a reduction of the electrical resistivity was also found. This trend, shown in Fig. 2b for samples deposited at both 180 °C and room temperature, likely results from the increase of the metallic content in low-pressure samples and maybe, as a minor effect, from the reduction of the film porosity (discussed below) as the sputtering pressure is decreased. The average resistivity values for each pressure are reported in Table 1.

In addition to the changes in samples stoichiometry and electrical properties, microstructural and morphological differences were also found in samples produced at different pressures.

XRD patterns are shown in Fig. 3. For the two samples produced at 1 and 0.5 Pa a crystalline MoS_2 phase is detected, whereas at lower pressure (0.11 Pa) an amorphous material is obtained. The (002)

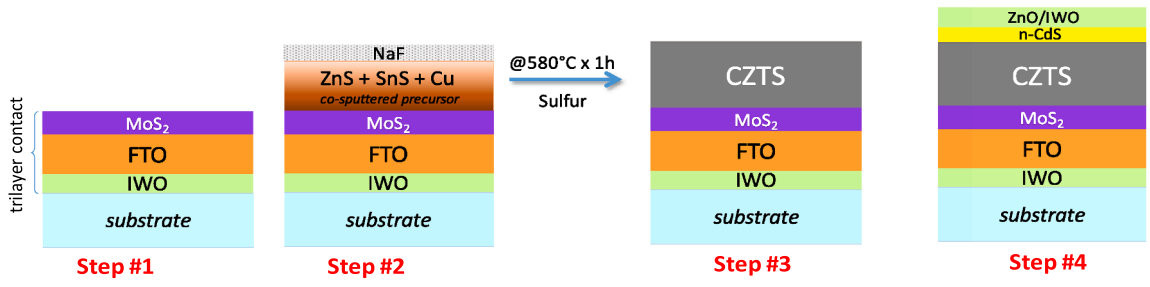

Fig. 1. Scheme of the fabrication process of the CZTS top cell onto MoS_2:Nb/FTO/IWO trilayer contact.

Table 1
Sputtering deposition conditions of MoS_2:Nb thin films: pressure (P), RF Power, nominal/actual deposition temperature (Tdep); thickness (d), average resistivity, material density ($\rho_{measured}$) and porosity (derived from weight measurements (exp) and from optical simulations (sim)).

MoS_2 sample type	P(Ar) (Pa)	RF-Power (W)	Tdep (°C)	d (nm)	resistivity (Ω cm)	$\rho_{measured}$ (g/cm^3)	porosity (exp) (%)	porosity (sim) (%)
MoS2-P1	**0.11**	150	180	170	0.002	5.2 ± 0.2	< 0	≈ 0
MoS2-P2	**0.5**	150	180	180	0.1	4.3 ± 0.2	10–20	≈ 10
MoS2-P3	**1.0**	150	180	220	0.3	3.8 ± 0.2	20–30	≈ 20

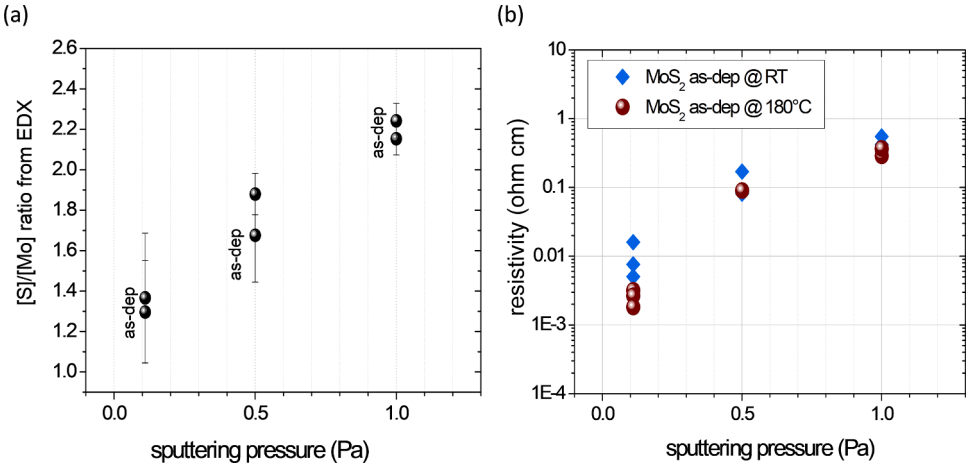

Fig. 2. (a) Chemical composition ([S]/[Mo] ratio) derived from EDX measurements and (b) electrical resistivity of as-deposited MoS_2:Nb films on borosilicate glass substrates at room temperature and at 180 °C.

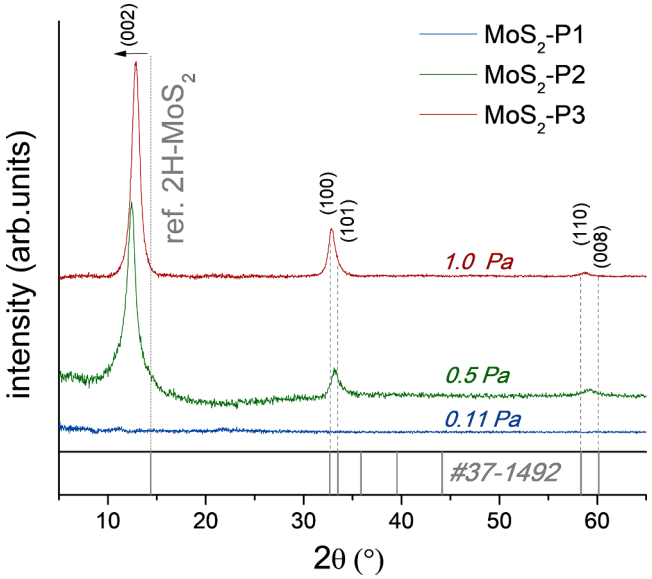

Fig. 3. XRD pattern of three MoS_2:Nb films deposited on BSG substrate at different sputtering pressure.

diffraction peak is shifted toward lower degree compared to the (002) peak position of 2H-MoS_2 bulk sample (14.38° – JCPDS file number: 37–1492), revealing an increase of the inter-layer distance (δ, Table 2) along the c-axis as the deposition pressure decreases from 1 to 0.5 Pa.

A similar shift of the (002) peak was often reported by other authors in the literature [26–28] for both thin films and nanoparticles [29] and it was typically ascribed to the intercalation of ions and molecules between MoS_2 layers, as well as to crystal defects or strain owing to curvature of the layers [29]. Sodium intercalation could likely account for the lattice expansion observed in our film since a Na signal (coming from

Table 2
Interlayer distance (δ) along the c-axis derived from the shift of the XRD (002) peak in MoS_2:Nb samples produced at different pressures. The inter-layer spacing δ was calculated using the Bragg's Law $n\lambda = 2\delta sin\theta$, where n is the diffraction order, λ is the wavelength of the radiation source and θ is the glancing angle.

sample type	press (Pa)	δ (Å)
MoS2 - P1	0.11	Amorphous
MoS2 - P2	0.5	7.104
MoS2 - P3	1.0	6.860
bulk-ref. [26]	—	6.148

undesired target contamination) was detected by GDOES depth profile analysis of our materials (an example of element distribution is shown in Fig. 10b, revealing a clear signal from both Nb and Na). Nonetheless, Argon ions could also play a role in the observed lattice expansion, since Ar could be more easily incorporated into the growing films as the working pressure decreases, in accordance with the increasing value of the interlayer-spacing δ.

It must be noted that a contribution to the shift of the (002) peak could be also given by the presence of different MoS_2 polymorphs like the metastable 1T-MoS_2 phase [28,30,31], which could not be excluded on the base of XRD only. The coexistence of different polymorphs was for example observed by in-situ STEM analysis in ref [32]. However, the XPS analyses discussed below, despite limited to a narrow surface region, seems to suggest the 2H-MoS_2 as the main phase present in our samples.

It is worth noticing that, compared to a MoS_2 bulk crystal, the lattice expansion in thin films should imply a decrease in material density. This correlation is reported, for example, in the work by Kaindl et al. [27], where sputtered films with expanded lattice are also found to exhibit density values between 3 and 4.3 g•cm^{-3}, significantly lower than the value expected for the MoS_2 bulk reference (4.99–5.06 g·cm^{-3} [27,33]).

Density ($\rho_{measured}$) measurements of the films revealed a monotonous

decrease of such parameter with increasing pressure (from 5.2 ± 0.2 g•cm^{-3}@0.11 Pa to 3.8 ± 0.2 g•cm^{-3}@1 Pa; Table 1), which cannot be ascribed to the lattice expansion (which in contrast would predict an opposite trend). This density variation can be more likely explained with the increase of the material porosity expected for increasing sputtering pressure, as a result of the reduced energy of the incident ions [34].

An estimation of the films porosity was obtained from the measured density ($\rho_{measured}$) and the theoretical value for the molybdenum disulfide (ρ_{theo}=5.06 g/cm^3 [33]) using the expression: $Porosity = 1 - \rho_{measured}/\rho_{theo}$ (Table 1). A porosity in the range of 20÷30 % was found for the film deposited at 1 Pa, whereas lower values are progressively found as the pressure is decreased to 0.5 Pa – with porosity around 10÷20 % – and to 0.11 Pa, when very compact films with completely suppressed porosity are obtained. In this case, the calculated porosity value is indeed close or slightly lower than zero, suggesting a compressive stress in MoS_2:Nb films deposited at the lowest pressure. This result, in accordance with the literature [35], is also compatible with delamination problems often observed in these last samples, showing poor adhesion on glass and silicon substrates, where formation of blisters is often observed after different thermal treatments.

Despite a reasonable error of about 5÷10 % associated to the provided porosity values (see Experimental), a reliable trend with the sputtering pressure is obtained, as also confirmed by the optical simulations results (Table 1) obtained by the software KSEMAWc [36] (details in the Appendix A).

Furthermore, planar and cross-sectional SEM views, reported in Fig. 4, seem to confirm the increase of the material porosity estimated for increasing sputtering pressure. In particular, a clear porous structure is observed for the highest-pressure sample, exhibiting a "lamellar-type morphology" similar to that reported in the literature for MoS_2 samples produced with similar sputtering conditions (see sample T3 in ref. [37]).

Fig. 5 reports the transmittance (T) and reflectance (R) spectra of samples deposited at different sputtering pressures. The absorption coefficient (α), derived as α= 1/d ln [(1-R)/T] (where d is the sample thickness), is also reported in Fig. 5c. The measurements show an increase of the transmittance as the Ar pressure increases, while the reflectance decreases. The reduction of R at low wavelengths for increasing pressure points to a reduction of the refractive index, in accordance with the decrease of the material density discussed before. The reduction of the film transparency with decreasing pressure is instead mainly due to an increase of the absorption coefficient with decreasing sputtering pressure, as a direct consequence of decrease of sulfur incorporation and material porosity. The corresponding Tauc's plots, calculated considering the expression for direct bandgap semiconductors ($\alpha(E) \sim \sqrt{(E-Eg)}/E$, where Eg is the optical bandgap), are reported in Fig. 5d. The indirect gap at about 1.2 eV [1,2] gives a weak absorption and can be neglected in this analysis. As-deposited samples produced at pressures equal or higher than 0.5 Pa show bandgap values (Eg) increasing from 1.70 to 1.74 eV, in fairly good agreement with the literature [3]. The Tauc's plot of the film produced at the lowest pressure is also reported for comparison, but the curve is not used to extract the optical bandgap since both the high α values (α>10^5 cm^{-1} for $E < 1$ eV) and the low transmittance ($T < 15$ %) point to a semi-metallic behavior, in accordance with its Mo-rich composition revealed by EDX analysis (Fig. 2a) and with the possible presence of minor inclusions of the metallic 1T phases.

3.2. Effect of sulfurization treatments on MoS_2:Nb films

MoS_2:Nb samples were subjected to a reactive annealing in sulphur atmosphere (sulfurization) to investigate the effect of the sulphur incorporation on the material properties after this post-deposition treatment (PDT). Obviously, different PDT conditions can be chosen and properly optimized depending on the future applications and/or experimental requirements. In this work, experiments were conducted in view of MoS_2:Nb applications as back contact in CZTS solar cells, where the absorber growth process typically requires sulfurization treatments at temperatures higher than 550–560 °C. If used as back-contact, the MoS_2:Nb layer will indirectly undergo a similar treatment. Therefore, two different sulfurization processes, similar to those used for CZTS, were used for the MoS_2:Nb films.

Both treatments were performed in a custom-made system (by IONVAC PROCESS s.r.l.) equipped with a vacuum chamber containing a graphite furnace (of 1000 cm^{3}vol) and a sulphur source of 15 cm^{3}vol, which is a separate cylindrical graphite chamber where sulfur pellets are placed and can be heated at a chosen temperature (270 °C was set in this work). The samples are placed inside the graphite furnace, where sulfur vapors are introduced by a N_2 carrier gas (pulsed flux 0.8 l/min with cycle on/off = 3 s/7 s) through a 6 cm long graphite tube (5 mm diameter) connecting the furnace with the sulfur source. The graphite furnace outlet can be kept either closed or connected to the external atmosphere through an outlet valve, allowing processes under continuous gas flux.

Both processes used in this work start with an initial annealing step of the samples of 15 min at 300 °C (heating rate of 20 K/min), followed by a second step of 60 min at 580 °C (same heating rate of 20 K/min). They differ in the amount of sulfur introduced into the furnace and in the permanence time, as illustrated in Fig. 6. The first process is a "softer" treatment, labelled as "*soft-sulf*", performed keeping the exit valve closed. The sulfur vapors are introduced into the chamber for a limited duration (approximately 15 min), beginning when the sample reaches 250 °C, to avoid undesired condensation over the "colder" samples, and stopping at the end of the plateau at 300 °C (see Fig. 6– orange profile). Then the sulfur heater is turned off, the carrier gas is stopped, and the

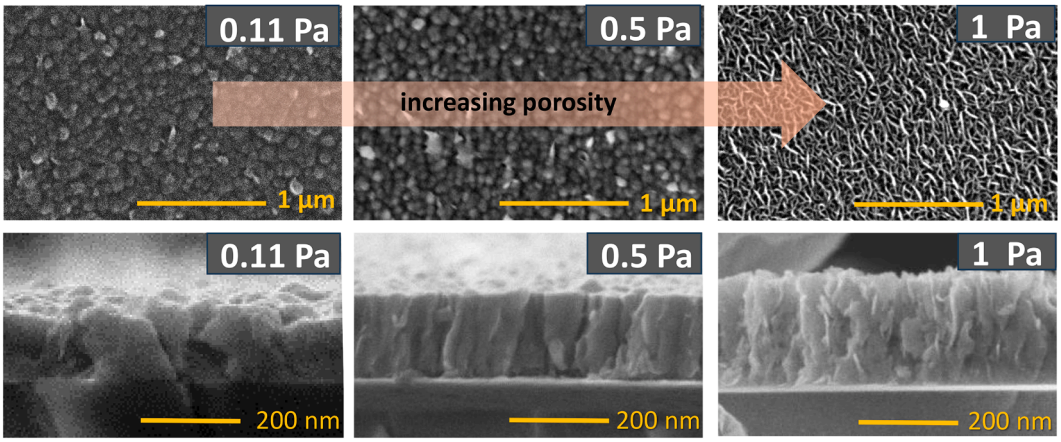

Fig. 4. Planar view and cross-sectional SEM images of as-deposited MoS_2:Nb films grown at different sputtering pressures with RF-power 150 W.

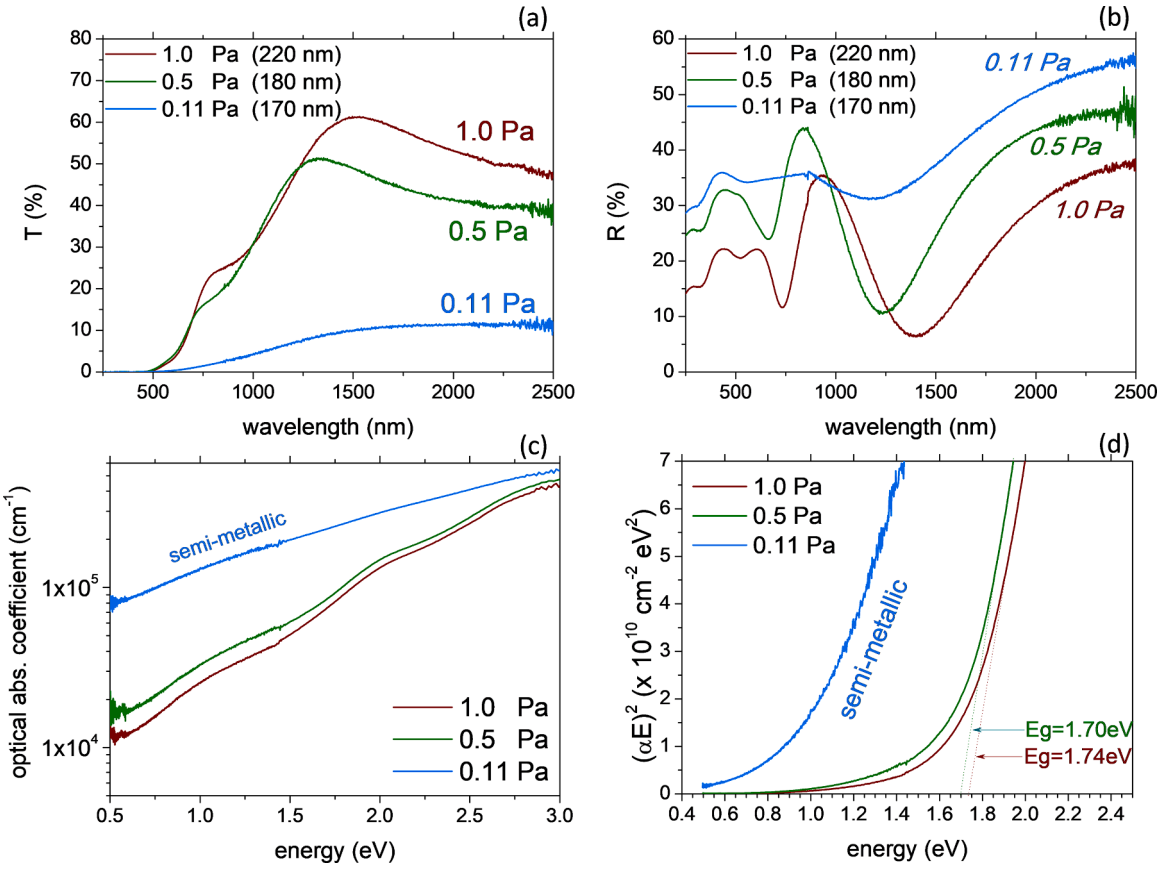

Fig. 5. Transmittance (a), Reflectance (b), absorption coefficient spectra (c) and Tauc's Plot (d) of as-deposited MoS_2:Nb film grown at different Ar-sputtering pressures.

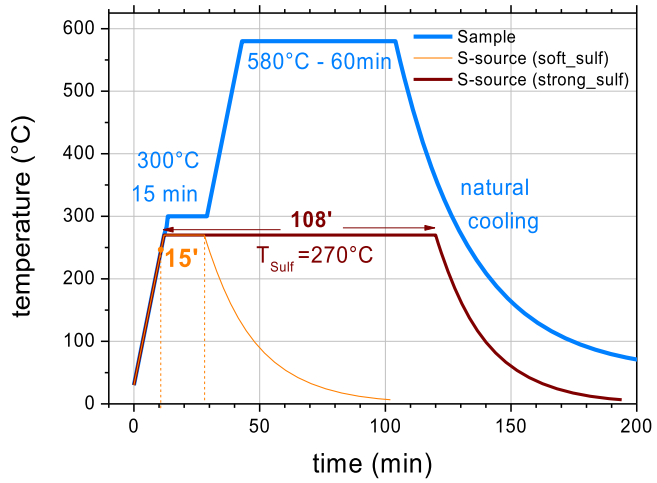

Fig. 6. Heating ramp of sample and sulfur source set during the sulfurization treatments (soft-sulf and strong-sulf) used in this work.

rest of the process continues in an almost static N_2/S atmosphere as the sulfurization chamber is kept closed during the entire treatment. The system pressure is set to 7×10^4 Pa at the beginning of the process (pure N_2 gas at RT), then raises to about 9.5×10^4 Pa at the end of the first plateau at 300 °C ($N_2 + S_{vapor}$) and reaches a constant value around 1.1×10^5 Pa during the final step at 580 °C. The second sulfurization treatment is a "stronger" process, labelled as "*strong-sulf*", which differs from the former in the higher sulphur supply. The carrier gas is fluxed inside the furnace from the moment when the samples reach 250 °C and for 108 min, until the end of the plateau at 580 °C (Fig. 6– dark red profile). To allow a continuous flux in the chamber avoiding over-pressure problems, the outlet valve of the system is kept open and the total working pressure is kept constant at 10^5 Pa during all the process.

Chemical, electrical, optical and microstructural characterizations of all the samples were performed after both sulfurization processes.

The results of EDX measurements are shown in Fig. 7. The softer treatment (*soft-sulf* – green squares in the plots) was found to lead only to a small increase of the [S]/[Mo] ratio compared to the as-deposited values and it was unable to produce a complete sulfurization of the

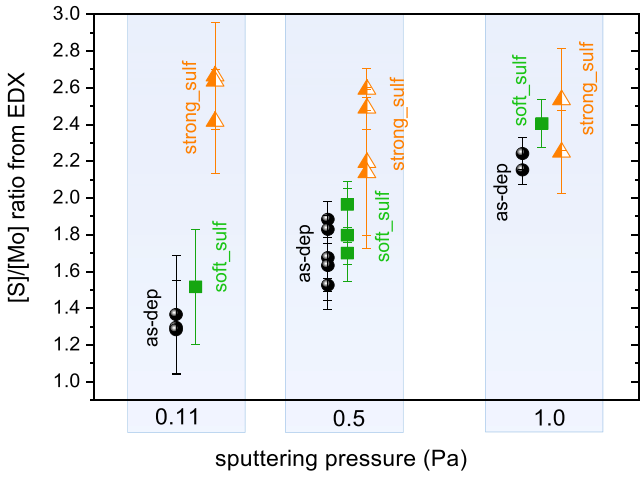

Fig. 7. [S]/[Mo] ratio measured in MoS_2:Nb films, as-deposited and after the two *soft-sulf* and *strong-sulf* PDTs.

(heavily or lightly) Mo-rich films produced at the lowest or intermediate pressures. A complete sulfur incorporation is instead found in all the samples after the stronger treatment (*strong-sulf* – orange triangles in the plot), leading to [S]/[Mo] ratios even higher than 2. For a deposition pressure of 1 Pa only a moderate increase of the sulfur content is detected after the treatments since the as-deposited films already show a [S]/[Mo] ratio close to or slightly larger than 2.

Even if the observed [S]/[Mo] ratios may be overestimated, values exceeding 2 could indicate the presence of elemental sulfur or the formation of S-rich phases [38]. Such phases cannot be identified using XRD, as no crystalline phases have been reported in the literature for molybdenum sulfides with [S]/[Mo]>2, (such as MoS_3 [39–41], Mo_3S_{13} [42]) and any potential sulfur cluster would likely be amorphous.

In order to clarify the nature of these samples, XPS measurements were performed. As an example, Fig. 8 reports the XPS spectra of Mo3d and S2p levels measured in a MoS_2:Nb film deposited at 1 Pa and subjected to the soft-sulfurization treatment. Almost identical spectra are obtained on the same sample after the strong sulfurization process, whereas slightly larger peaks are observed in the as-dep sample, as shown in Fig. B2.

The Mo3d spectrum (Fig. 8a) is dominated by two bands at binding energy (BE) of 229.05 eV and 232.22 eV (blue curves), corresponding to the doublet (Mo $3d_{5/2}$ and Mo $3d_{3/2}$) of the Mo^{4+} in the 2H-MoS_2 lattice [28,43,41,44]. The other two small contributions observed at 230.0 and 233.22 eV (magenta curves) could indicate an amorphous Mo_2S_5 phase [43,45,46] (around 5 % from semiquantitative analysis) whereas the band at 226.32 eV (orange curve) can be assigned to S^{2-} (S 2s orbital) in the MoS_2 phase [45,46]. We note that the Mo_2S_5 phase can be detected only looking at the Mo3d spectrum because its S2p bands cannot be assigned due to lack of relevant XPS data in the literature [43,45,46].

The analysis of the Mo3d spectra helps to identify the 2H-MoS_2 as the main phase present in our samples, excluding the formation of the 1T-phase (at least in the 2–10 nm thick top region probed by XPS) which could be postulated based on the XRD data discussed before. Indeed, according to the literature, the binding energies of the Mo3d doublet in the 1T-MoS_2 phase would be shifted of about 0.9 eV to lower values compared to 2H-MoS_2 [28,44,47]: for example in the work by Cheng et al. the reported BE of Mo $3d_{5/2}$ and Mo $3d_{3/2}$ are 228.25 and 231.35 eV for the 1T phase and 229.15 and 232.25 eV for the 2H phase [44]; Similarly, Liu et al. [48] reported the two Mo $3d_{5/2}$ and Mo $3d_{3/2}$ characteristic peaks at ≈228.1 and ≈231.1 eV for the 1T-MoS_2, much lower than those of 2H-MoS_2 at ≈229.5 and 232 eV.

The S2p spectrum shown in Fig. 8b can be modelled with two main bands (blue curves) at BE around 161.9 eV and 163.1 eV, corresponding to the S2p doublet (S^{2-}) in 2H-MoS_2, in accordance with the literature [46,44,28,43,45]. These data allow excluding the presence of the 1T-MoS_2 phase which would instead exhibit a downshift of about 0.9 eV in the BE values with respect to the 2H-MoS_2 phase (for example the $S2p_{3/2}/S2p_{1/2}$ characteristic peaks are reported at about 161.05/162.2 eV for the 1T-MoS_2 and at 161.9/163.1 eV for the 2H-MoS_2 [44]).

To improve the fit quality, in addition to the main S2p bands in MoS_2, other contributions at higher BE have to be considered, related to Mo_3S_{13} or MoS_3, [41,42]. The Mo_3S_{13} phase was considered as a first option because, compared to other compounds, it would help to better explain the sulphur excess revealed by EDX. The S2p spectrum decomposition in Fig. 8b includes the two Mo_3S_{13} S2p doublets at 162.3/163.5 (S_2^{2-} terminal – green curve) and at 163.6/164.8 (S_2^{2-} bridging or S^{2-} apical – green dashed curve) [42]), even though the contribution of the latter doublet is negligible. This analysis would predict an amount of Mo_3S_{13} around 15 % which (together with 5 % of Mo_2S_5) would allow explaining the sulphur excess in the sample. However, this analysis is not the only possible one, as a similar fit quality for the S2p spectrum can be also obtained considering the MoS_3, with doublets at 162.9/164.1 (S_2^{2-} bridging o S^{2-} apical) and 161.6/162.8 (S_2^{2-} terminal o S^{2-}) [41], even though its estimated amount would not be enough to explain the sulphur excess.

It is worth noticing that the analysis of the Mo3d spectrum is not helpful to distinguish neither Mo_3S_{13} nor MoS_3 from MoS_2 as the Mo is in the same oxidation state (4+) in all compounds [42,40,41]. Due to the arbitrariness of the XPS data fits, it is impossible to obtain a reliable identification of the amorphous phases present in the samples and a quantitative estimation of their amount. Anyway, for both models the calculated semiquantitative S/Mo ratio is around 2.2, in reasonable agreement with the EDX data. The presence of elemental sulphur can be neglected as signals at higher energies (164.1/165.2) should be observed. Finally, we can exclude the presence of both SO_2, which would give a signal at 167/168 eV [49] and Na_2SO_4, which would give a contribution from S^{6+}species at about 168.6 eV [50].

Although the XPS analysis is only sensitive to the first 2–10 nm of the surface of the sample, the general deductions about the presence of sulfur-rich phases can most likely be applied to the bulk of the sample, as suggested by the EDX data revealing a large sulfur excess.

The XRD technique was used to characterize the crystalline MoS_2 phase present in our samples and its evolution after the thermal treatments. Fig. 9 reports the diffractograms measured for a film deposited at 0.5 Pa and subjected to different thermal treatments. Similar results are obtained for samples deposited at 1 Pa. Compared to the as-dep film, a progressive shift of the (002) peak toward higher 2θ values is observed (Table 3), suggesting a reduction of the interlayer distance which becomes more similar to the nominal value of the bulk samples (6.147 Å [26,27]). A similar shift is also observed in samples deposited at 1 Pa, whereas the samples deposited at 0.11 Pa remain amorphous even after the sulfurization treatments.

Based on our previous hypothesis, which suggests that impurity intercalation is responsible for the increase of the interplanar distance, the observed shift of the (002) peak towards higher angles after the

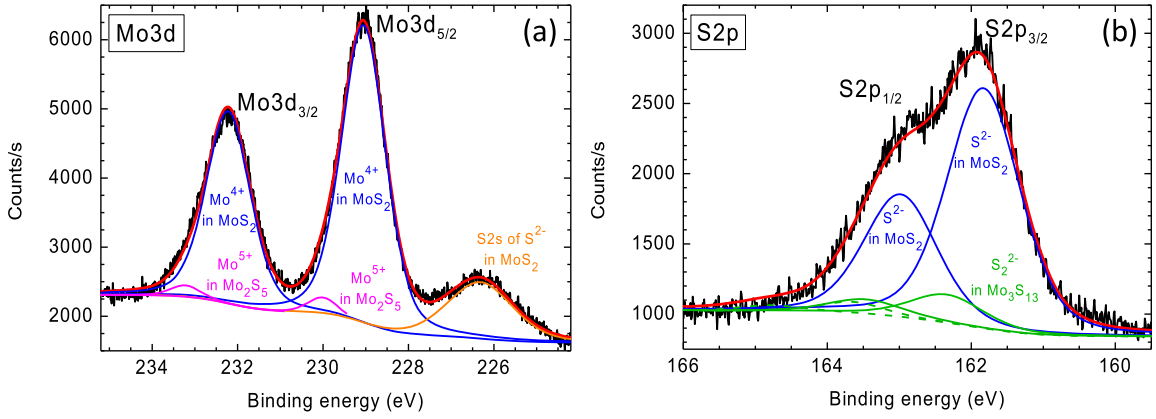

Fig. 8. XPS spectra of Mo3d (a) and S2p (b) measured in a MoS_2:Nb thin films deposited at 1 Pa and subjected to soft sulfurization.

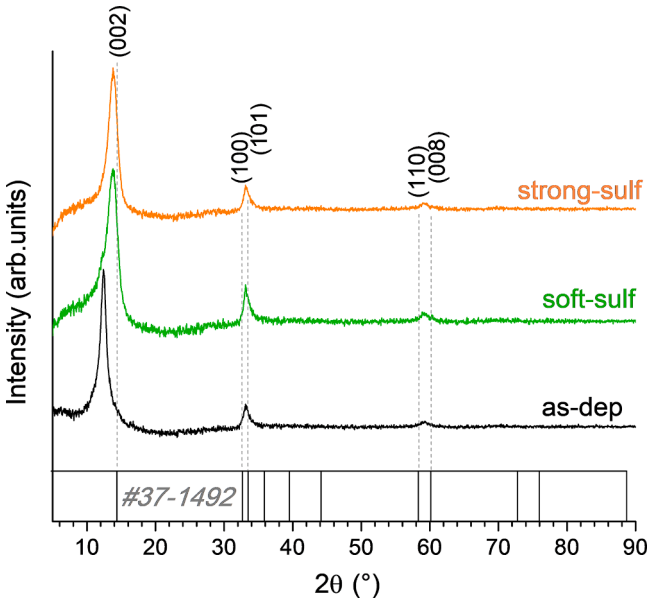

Fig. 9. XRD pattern of a MoS_2 sample deposited at 0.5 Pa on borosilicate glass and measured after different treatments.

Table 3
Interlayer distance (δ) along the c-axes derived from the XRD patterns of a MoS_2:Nb film deposited at 0.5 Pa on BSG and subjected to the *soft-* and the *strong-* sulfurization treatments.

sample treatment	δ(Å)
As-dep	7.129
soft-sulf	6.392
strong-sulf	6.331
bulk-ref [27]	6.147

thermal treatments may indicate an impurity out-diffusion.

This hypothesis seems to be confirmed by GDOES measurements, as those reported as an example in Fig. 10a and referring to films deposited on borosilicate glass substrates. Sodium contaminations were indeed detected by GDOES in as-deposited materials, where a clear Na signal can be observed inside the MoS_2:Nb films, with a higher accumulation at the MoS_2:Nb/Si interface. The Na content was found to progressively decrease after the two sulfurization processes, thus confirming its out-diffusion. Additional experiments proved that this Na contamination doesn't arise from substrates or system contaminations, but from the sputtering target itself. Concerning the elements profiles in Fig. 10a, it has to be noted that the signals recorded during the initial seconds of the measurement (sputtering time from 0 to 1–1.5 s) may be affected by preferential sputtering effects or related to the typical initial instability of the GDOES plasma. Therefore, the apparent enhanced S content detected at the surface (peak between 0 and 1 s), as well as the low Mo signal in the same region, might not indicate a truly sulfur-rich surface but could simply be due to measurement artefacts.

Furthermore, we note that the Nb signal in samples deposited on BSG substrates was typically found very weak and noisy because of the low GDOES sputtering rate, combined with low Nb content and detector sensitivity. Therefore, Nb profile is not shown in Fig. 10a. Anyway, an evidence of the Nb incorporation inside the MoS_2:Nb films was obtained from GDOES measurements on samples grown on Silicon wafer (Fig. 10b), where the Nb signal is better detected thanks to the higher GDOES sputtering rate (allowed by the conductive nature of the Silicon substrate).

In Fig. 11, the transmittance and reflectance spectra measured after the two sulfurization treatments are compared with those of the as-deposited film for each sputtering pressure. In the same figure, the derived absorption coefficient spectra and Tauc's plots are also reported.

The sample deposited at the lowest pressure (0.11 Pa) shows only a slight increase of the transmittance (from about 10 to 25 %) after the soft-sulfurization treatment, as expected from the EDX results indicating a large sulfur deficit still present in the film. For the sample produced at intermediate pressure (0.5 Pa), a similar optical behavior is found after both *soft-sulf* and *strong-sulf* treatments, since after the *soft-sulf* the chemical composition is already close to the stoichiometric one and only a slight transparency improvement is expected after the stronger treatment. For the sample grown at 1 Pa the improved transparency has to be only imputed to a reduction of sub-bandgap defect absorption since the chemical composition remain almost unchanged. The reflectance spectra of all the samples do not show any change at low wavelengths, thus implying no change in refractive index and porosity after sulfurization.

The bandgap energy of the analysed samples can be obtained from the Tauc's plots calculated with the same expression used before for direct bandgap semiconductors. For the samples at the lowest pressure a semiconductive behavior is expected only after *strong-sulf*, so the curves for the as-deposited and *soft-sulf* films (with Mo-rich composition and semi-metallic behavior) cannot be used to define an optical bandgap.

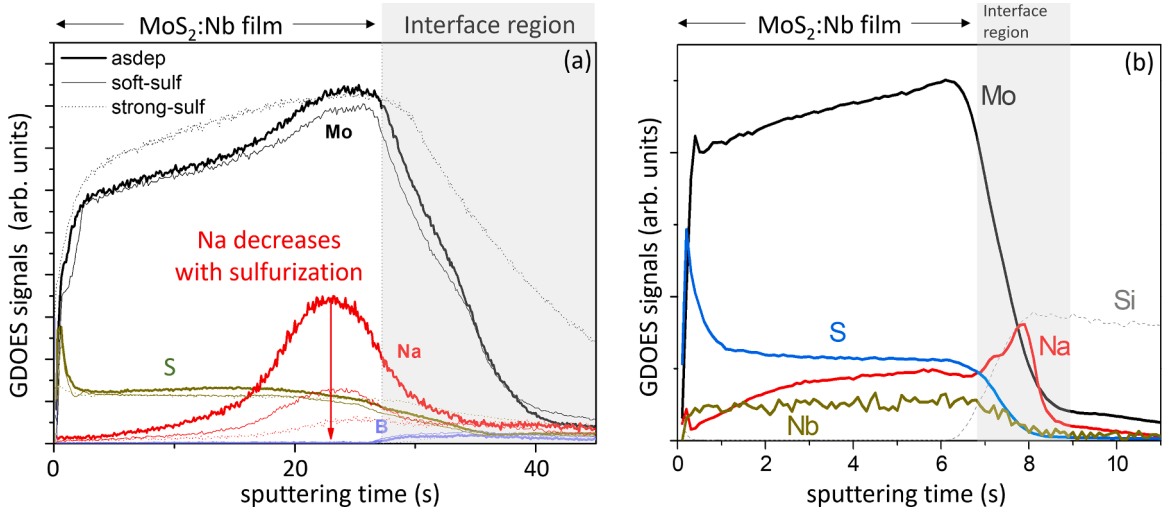

Fig. 10. Elements profiles from GDOES measurements of MoS_2:Nb films sputtered at 0.5 Pa on (a) borosilicate glass (BSG) in the as-deposited state and after different sulfurization treatments, and (b) as-deposited on Silicon wafer.

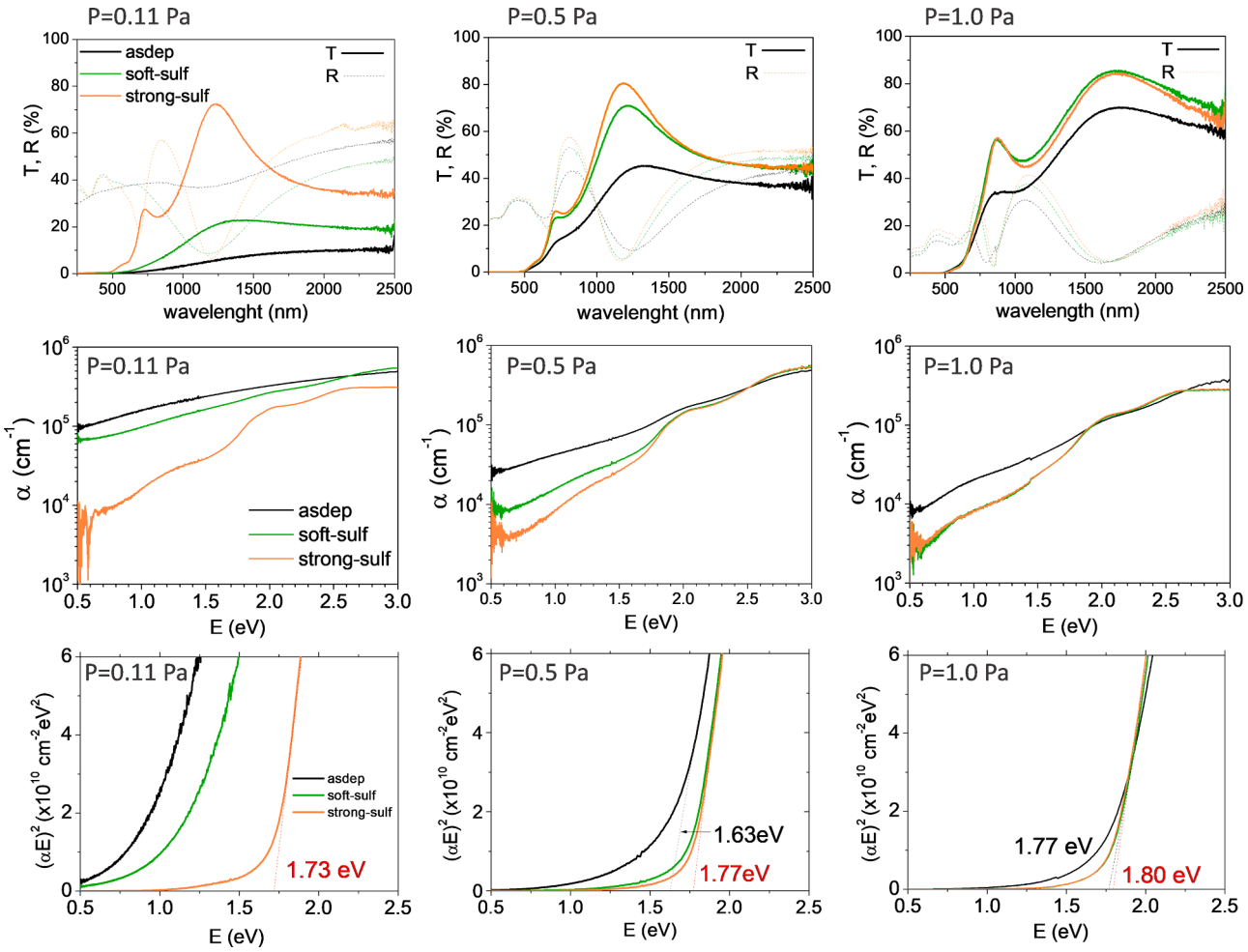

Fig. 11. Variation of T and R (upper panel), absorption coefficient (central panel) and Tauc's Plot (lower panel) of MoS_2:Nb film deposited at different sputtering pressures after different sulfurization treatments.

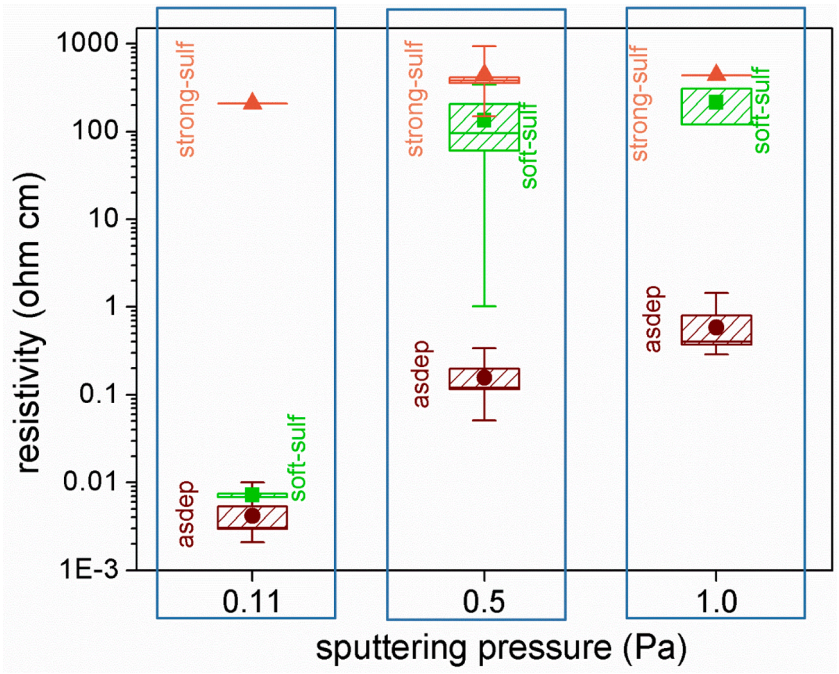

Fig. 12. Evolution of the electrical resistivity of MoS_2:Nb films after the *soft-sulf* and *strong-sulf* sulfurization treatments.

Nevertheless, the latter curves are reported to show the variation of the optical absorption induced by the progressive sulfur incorporation. As shown in the plots, the Eg values found in all the samples with the correct stoichiometry are in the range 1.7–1.8 eV, in fairly good agreement with the literature value for the monocrystalline samples [3].

3.3. Electrical properties of as-deposited and sulfurized MoS_2:Nb films

Samples resistivity measured by four-points probe after different treatments are reported in Fig. 12. The change of the electrical resistivity with the deposition pressure observed in the as-dep materials (dark-red circles) was discussed previously (Fig. 2b) and correlated to the different film microstructure and composition. Independently from the deposition pressure, the resistivity shows a progressive increase after the soft- (green-squares) and the strong- (orange triangles) sulfurization treatments, with a clear correlation to the increase of the sulfur incorporation revealed by EDX data in Fig. 7. In particular, after the soft-sulfurization treatment, the resistivity of samples produced at 0.11 Pa shows a negligible increase compared to the as-dep films, with values lower than 0.01 Ω•cm, pointing to a semi-metallic behavior, as expected from the still large sulfur deficit (Fig. 7) and also from the optical characterization previously discussed (Fig. 11). Resistivities higher than 10^2 Ω•cm are instead measured in these samples after the *strong-sulf*, when the films are completely (and even over-) sulfurized, showing semiconductive properties.

Unlike the samples grown at the lowest pressure, the samples produced at both 0.5 and 1 Pa show a first significant increase of their resistivity already after the *soft-sulf*, with average values around 100–200 Ω•cm (about three orders of magnitude higher compared to the as-dep films), and a further increase is observed after the stronger treatment, leading to resistivity values between 400 and 500 Ω•cm.

Assuming that the materials are n-type, the observed increase of resistivity with the increase of sulfur incorporation could be ascribed to a reduction of the concentration of sulfur vacancies (V_S) as they are often

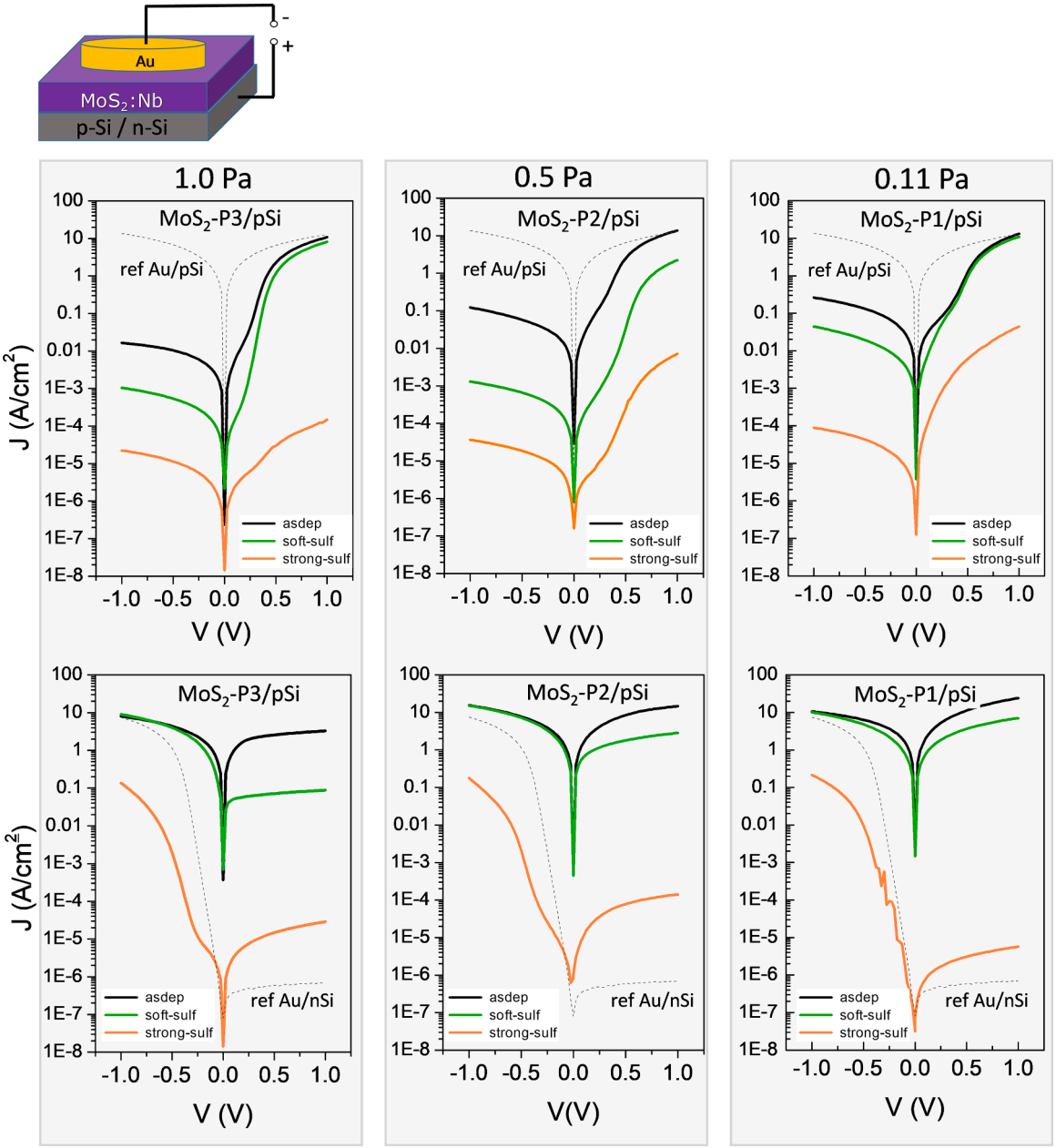

Fig. 13. J-V curves of MoS2:Nb/c-Si heterojunctions based on p-type (top panel) and n-type (bottom panel) silicon wafers. The dotted lines refer to measurements on the junctions between Au and p- or n-silicon. The polarity of the applied voltage is depicted in the upper scheme.

reported to be donor defects [5–7], despite some controversies are found in the literature [8]. A similar dependence of the conductivity on the sulfur content was also reported by other authors in the literature [6,7]. On the other hand, the effect of possible extrinsic defects cannot be excluded. Na was indeed reported to behave like a donor defect producing an n-type doping [19,20]. Therefore, the sodium out-diffusion could also play a role in the resistivity increase after thermal treatments.

On the contrary, assuming a p-type conduction of the materials, the resistivity changes could be explained only assuming that the sulfur vacancy is an acceptor, and the effect of sodium is of minor importance.

Hall measurements would be obviously needed to clarify the conductivity type and the role of possible mobility changes. However, Hall measurements performed with our system (0.5 Tesla) gave no meaningful results due to a negligible Hall voltage. This could be likely imputed to the presence of an amorphous fraction as well as to sample inhomogeneity. Indeed, in the paper by Mc Donnell [51] it was reported that it is possible to detect regions with different conductivity type in a single sample.

Due to these difficulties, the electrical behavior of MoS_2:Nb films was indirectly investigated by measuring the J-V curves of MoS_2:Nb/c-Si heterojunctions, produced using both n-type and p-type Si wafer. The wafers were deoxidized in HF 1 % chemical bath before the MoS_2:Nb sputtering deposition. The top and the rear electric contacts were then respectively formed by evaporating gold dots (Au dot diameter 1 mm) on the MoS_2:Nb surface and by using an In-Ga eutectic solution on the back side of the Si wafer. The devices were characterized soon after the MoS_2:Nb deposition (as-deposited) and after the sulfurization treatments (*soft-sulf, strong-sulf*).

Fig. 13 shows the J-V curves of all devices obtained on p-type (upper panel) and n-type (bottom panel) Si wafers, using a MoS_2:Nb top-layer deposited at different sputtering pressures. The dotted lines refer to an Au/Si junctions, made on both p- and n-type wafers, and are shown to clarify that the MoS_2:Nb /Si JV curves are not affected by possible shunts effects between the Au electric contact and silicon. The interpretation of these results is quite complex since interface dipoles or defects can strongly affect the band alignment and the junction properties. Anyway, it is apparent that as-deposited MoS_2:Nb films form a barrier on p-type silicon and give rise to a nearly ohmic contact on n-type silicon. Moreover, the increase of sulfur incorporation leads to the formation of a barrier on n-type silicon and to a decrease of the J-V curve asymmetry on p-type. These trends suggest, despite the doping with Niobium, an n-type conductivity of the as-deposited MoS_2:Nb films and an increase of the work function upon sulfurization. The same trend supports also the donor character of sulfur vacancies (V_S) and the possible relevance of sodium as extrinsic donor dopant.

Other experiments in the literature showed a similar trend of the conductivity with the stoichiometry: for example Mc Donnell et al. [51] showed that n-type and p-type regions can coexist in the same sample and used localized XPS to show that [S]/[Mo]=1.8 in the n-type region while [S]/[Mo]=2.3 in the p-type region, pointing to a donor-like behavior of the V_S [5–7]. It must be noted that ab-initio calculations [8] suggest instead that V_S behaves like a deep acceptor.

To get further information on the Fermi level position, a MoS_2:Nb film deposited at 1 Pa was selected for UPS measurements due to the nearly correct stoichiometry in the as-deposited state and the good adhesion even after the sulfurization treatments.

The UPS results are shown in Fig. 14. The low kinetic energy portion of the UPS spectrum can be used to extract the work function value while the high kinetic energy portion provides an estimation of the distance between the Fermi level and the top of the valence band (E_F-VBM). It can be seen that the WF increases from 4.9 to 5.1 eV with increasing sulfur incorporation. However, the three spectra are coincident for energies above 19.5 eV and therefore the E_F-VBM value remains unchanged at about 0.8 eV, pointing to n-type or nearly intrinsic materials.

The simplest hypothesis to explain these results could be that the sulfur incorporation changes only the electron affinity of the MoS_2:Nb without changing the Fermi level position (E_F-VBM). However, with this picture the changes in the electrical resistivity (Fig. 12) would be hard to explain.

Another possible explanation is based on the hypothesis of the coexistence, within the same sample, of regions with different doping levels as suggested by other authors in the literature [51]. In this picture, in the low kinetic energy region, the spectrum would be dominated by the photoemission from the regions with the lower WF (n^+ regions), which mask the contribution from the less (n^-) doped regions with higher WF. On the contrary, in the high kinetic energy region (around 20 eV), the UPS spectrum would be dominated by the photoemission from the regions with lower E_F-VBM value (less n-type doped). Under this hypothesis, the results in Fig. 14b (showing a very similar onset for both as-dep and sulfurized films) indicate that the E_F position in the n^--regions remains almost unchanged after the sulfurization treatments, which in contrast affect the E_F-VBM distance only in the n^+-regions (Fig. 14a) by reducing the donor defects concentration. This picture would explain the increase in both the film resistivity and the barrier at the MoS_2:Nb /nSi interface leading to a rectifying behavior of the contact (in agreement with the results in Figs. 12 and 13).

The sulfurization would therefore produce a material with a lower and more homogeneous conductivity. It is interesting to note that this picture would be in accordance with XPS data in Fig. B2, showing broader Mo3d peaks in the as-deposited sample.

It must be noted that a work function as large as 4.9 eV would not be compatible with the ohmic behavior of the MoS_2:Nb /n-Si junctions if the simple Electron Affinity Rule is supposed to be valid: a substantial interface dipole has to be hypothesized.

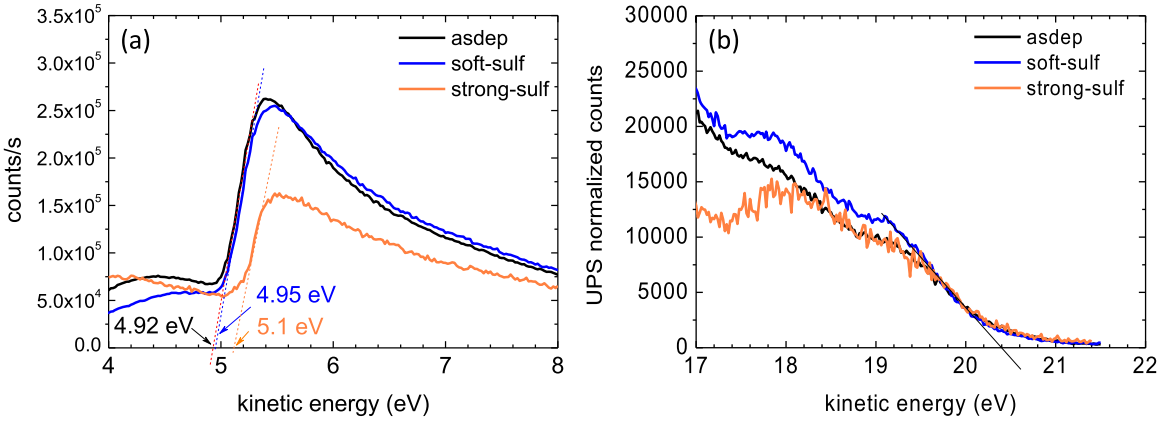

Fig. 14. Low (a) and high (b) kinetic energy portion of the UPS spectrum of a MoS_2:Nb film deposited at 1 Pa.

3.4. Application of MoS_2:Nb thin films in CZTS solar cells and CZTS/Si tandem devices

The sputtered MoS_2:Nb films were tested as hole transport layers in CZTS/c-Si tandem solar cells. A similar attempt was already made by our group using a MoS_2 layer obtained through the sulfurization of a metallic Mo layer. That work produced the first working monolithic CZTS/Si tandem cell [18] and a MoS_2 /FTO/ZnO trilayer was employed as an intermediate contact between the CZTS and a silicon cell fabricated using a wafer with flat front surface. The Fluorine-doped Tin Oxide (FTO) was introduced, thanks to its good chemical stability, to protect the bottom stack from the reactive atmosphere during the CZTS sulfurization. The ZnO layer was instead used to get a good ohmic contact with the underlying n-type silicon. This process produced working tandem devices on flat c-Si wafers, but it failed on textured c-Si wafers, due to the formation of SnS_x platelets on the trilayer surface during the Mo layer sulfurization. These platelets extend for several microns out of the trilayer and cause a fatal shunting of the top cell. The use of a much softer sulfurization process is not a viable solution since this cannot guarantee the complete transformation of Mo into MoS_2.

The deposition of the MoS_2:Nb layer directly on TCOs by RF sputtering gives the double advantage of ensuring a better control of both the thickness and transparency of this layer and of preserving the TCO from degradation, avoiding also the formation of SnSx platelets on textured wafers. This is an important advantage since it could allow to fabricate tandem devices using silicon bottom cells with textured front side. This type of silicon cells is the standard in the PV industry, having higher currents due to the reduced front reflectance and enhanced light trapping.

A further improvement of the MoS_2:Nb/FTO/IWO contact trilayer structure used in this work is the replacement of the ZnO layer with a Tungsten-doped Indium Oxide (IWO) which plays an analogous role from an electrical point of view but, due to its higher transparency, allows the deposition of thicker layers (around 300 nm) helping the blocking action against elements diffusion (in particular Copper, as reported in [52,53]).

As a first test, CZTS absorbers were grown in parallel onto different MoS_2:Nb/FTO/IWO trilayer contacts on BSG for the optical and electrical characterizations. Since the CZTS growth process includes a sulfurization treatment at 580 ° C it was quite likely that the final MoS_2:Nb layers located under the CZTS could show optical properties similar to those reported in the previous sections for the sulfurized films.

MoS_2:Nb layers of about 30 nm were chosen in view of the device fabrication in order to reduce the undesired absorption in the region of interest for tandem application (750–1200 nm). The optical analysis indeed revealed that with such a MoS_2:Nb thickness the absorptance (1-R-T) expected for the bare trilayer stack in the device is as low as 5 % in this wavelength range (Fig. C1) and a quite good transparency (with absorptance around 20 % in the same region) is maintained even after the CZTS deposition, as revealed by the absorptance spectra in Fig. 15.

It must be pointed out that similar absorptances are obtained independently on the MoS_2:Nb deposition pressure, meaning that the sulfurization of the CZTS precursor is able to compensate the sulfur deficit in as-deposited MoS_2:Nb films, even in the case of the lowest deposition pressure (0.11 Pa), which instead gave films with low transmittance and high Mo content in the as-deposited state.

The electrical characterization of the CZTS/MoS_2:Nb/FTO/IWO/BSG samples was performed measuring the J-V curves between IWO and gold dots evaporated on CZTS. The J-V curve (not reported here) shows a nearly ohmic behavior with a contact resistance of about 0.4 Ω•cm^2, which correspond to a voltage loss lower than 10 mV in a typical tandem device with a 20 mA/cm^2 photocurrent. The ohmic behavior excludes the presence of a significant potential barrier at the CZTS/MoS_2:Nb interface. Note that this result could have also been promoted by possible impurity or metal interdiffusion.

These samples on glass were also completed as solar cells depositing a CdS/ZnO/IWO front contact and, even if plagued by severe adhesion problems, they showed the potentiality to give cells with efficiency comparable to reference devices grown on standard Mo back contact (about 5 % efficiency).

To show the potential application of sputtered MoS_2:Nb in CZTS/c-Si tandem devices fabricated on textured wafers we chose to use a MoS_2:Nb layer deposited at a sputtering pressure of 0.5 Pa with a thickness of about 30 nm since these parameters allow to obtain good electrical and mechanical contact with the top cell absorber and to maximize the radiation transmitted to the bottom Si cell. The SEM picture in Fig. 16 shows that in this way a good conformal coverage of the textured silicon device can be obtained.

Two different CZTS thicknesses of about 0.5 and 1 μm were tested for the complete tandem device, and the corresponding J-V characteristic and EQE are reported in Fig. 17. The highest efficiency (4.4 %) was obtained using a CZTS thickness of about 1 μm (Tandem1) and the quantum efficiency measurements show that the Jsc in this cell is limited by the current of the bottom silicon cell.

The CZTS thickness reduction to 0.5 μm (Tandem2) leads to a significant increase of the photocurrent of the Si bottom-cell to 9.6 mA/cm^2 but this improvement is not transferred to the tandem performances due to the decrease of the QY of the top cell. These findings are clearly due to

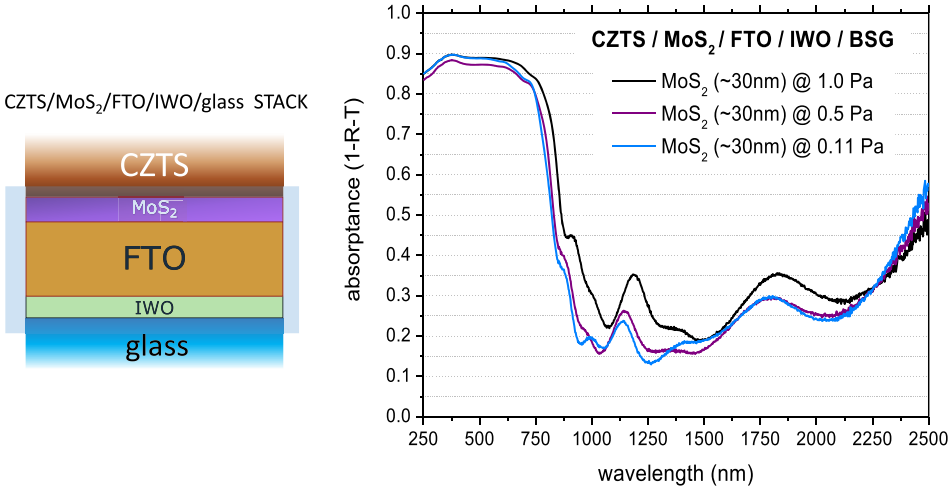

Fig. 15. Absorptance (1-R-T) of three CZTS/MoS_2:Nb /FTO/IWO stacks on BSG substrate, all with MoS_2:Nb thickness of about 30 nm but differing for the deposition pressure of the MoS_2:Nb layer.

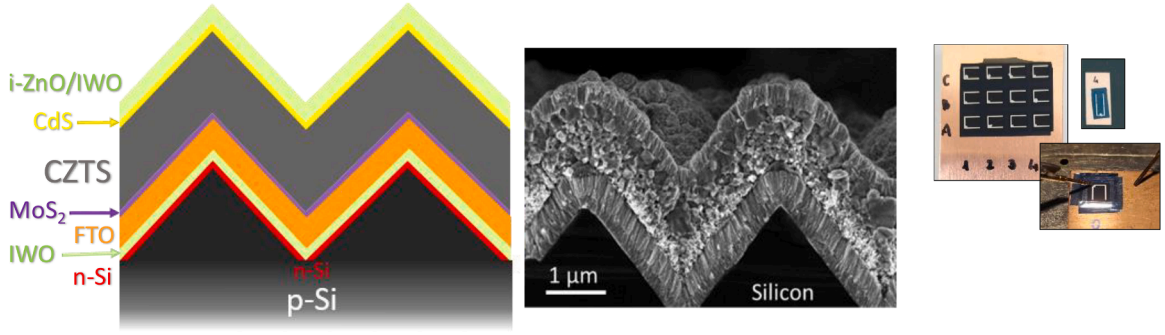

Fig. 16. Structure of the tandem device fabricated for this work. The SEM cross section shows the good conformal growth of the top layers. The photos on the right show the final device with the grid and the mask: the illuminated area is 0.25 cm^2.

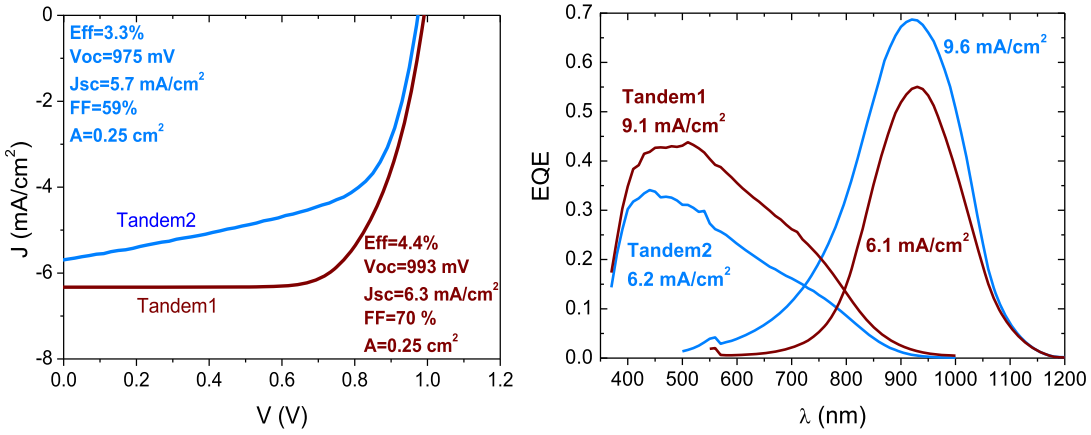

Fig. 17. J-V characteristic and Quantum Efficiency of two tandem solar cells with a different thickness of the top cell CZTS absorber: $d = 1$ µm in Tandem1 and $d = 0.5$ µm in cell Tandem2.

the lower quality of the CZTS film grown on textured substrates. If a Jsc greater than 9 mA/cm^2 could be restored optimizing the sulfurization process, efficiencies well in excess of 6 % would be achievable with the same optical performances of the different layers. On the other hand, a more significant efficiency increase necessarily requires an improvement of the top-cell Voc.

4. Conclusions

In this work we investigated the properties of MoS_2:Nb films deposited via magnetron RF sputtering in view of their application as IR-transparent contacts in tandem photovoltaic devices. We identified the Argon sputtering pressure as a crucial deposition parameter. Films grown at about 0.1 Pa exhibited compactness but lack of crystallinity, showing a significant sulfur deficit ([S]/[Mo]≈1.4) and a notable sub-bandgap optical absorptance. Materials with a stoichiometry ratio up to [S]/[Mo]≈2.2 were produced by increasing the Ar pressure to 1 Pa, yielding more transparent films, although with a rather porous morphology. Even if the XRD patterns of the samples deposited at 1 Pa showed a clear crystalline fraction, the XPS analysis revealed the presence of S-rich amorphous phases, compatible with stoichiometry ratios larger than 2. The UPS measurements showed a work function exceeding 4.9 eV and a value of EF-VBM≈0.8 eV, indicating that the 0.5 % Niobium doping of the target is not sufficiently high to produce p-type samples and that the combined effects of uncontrolled impurities and intrinsic defects lead instead to an n-type conductivity.

Post-deposition sulfurization treatments led to a work function increase beyond 5 eV, accompanied by an expected rise of the electrical resistivity, but not by a parallel decrease of EF-VBM values. A possible explanation was proposed supposing that the films are not-homogeneous but are rather composed by distinct regions with different levels of n-type doping and that only the most doped ones ($n+$ regions, with larger concentration of sulfur vacancies and/or Na impurities) are affected by the sulfurization process.

A similar increase in work function was expected in the CZTS/MoS_2:Nb junctions, when the sputtered MoS_2:Nb films are overcoated with the CZTS precursor and undergo the sulfurization step needed to obtain the polycrystalline CZTS absorber. The CZTS/MoS_2:Nb contacts demonstrated the desired ohmic characteristic and showed the potentiality to form complete CZTS solar cells with efficiency comparable with standard devices based on Mo contact.

Furthermore, employing MoS_2:Nb films deposited at an intermediate pressure (0.5 Pa), we fabricated CZTS/c-Si tandem devices on textured silicon solar cells. Despite achieving a modest maximum efficiency of 4.4 %, limited by CZTS film quality on textured substrates, the MoS_2:Nb/TCOs structure as intermediate contacts exhibited good optical transparency and electrical behavior.

CRediT authorship contribution statement

Claudia Malerba: Writing – review & editing, Writing – original draft, Validation, Methodology, Investigation, Conceptualization. **Matteo Valentini:** Writing – review & editing, Validation, Methodology, Investigation, Conceptualization. **Francesca Menchini:** Writing – review & editing, Validation, Investigation. **Daniele Mirabile Gattia:** Validation, Investigation. **Enrico Salza:** Validation. **Alberto Mittiga:** Writing – review & editing, Validation, Supervision, Methodology, Investigation, Funding acquisition, Conceptualization.

Declaration of competing interest

The authors declare that they have no known competing financial interests or personal relationships that could have appeared to influence the work reported in this paper.

Data availability

Data will be made available on request.

Acknowledgements

This work has received funding from the European Union H2020 Framework Programme under Grant Agreement no 952982 (Custom-Art) and it was also supported by the Italian Ministry of Economic Development in the framework of the Operating Agreement with ENEA for the Research on the Electric System.

Appendix

Appendix A: Optical simulations of sputtered MoS2 films with the software kSEMAWc

Optical simulations of sputtered MoS_2 films were performed using the software kSEMAWc [21], an open-source software for the analysis of Spectrophotometric (SP), Ellipsometric (ELI) and Photothermal Deflection Spectroscopy (PDS) measurements. The software can be used both to (1) simulate SP, ELI and PDS measurements of a multilayer structure, being known the thicknesses and the complex refractive indexes of each material composing the different layers, and to (2) calculate the complex refractive index and the thickness of a given layer from experimental measurements (SP, ELI, PDS), being known the thicknesses and the complex refractive indexes of all the other layers composing the structure. kSEMAWc uses a mathematical approach based on transfer matrices, particularly suitable for the case of multilayers: in addition to being able to treat coherent propagation and interference (for arbitrary incidence angles), it also allows to simulate the effects due to different types of non-ideal material properties, such as optical constants gradients along the film thickness, thickness inhomogeneity and roughness. The material porosity can be also taken into account by using the Effective Medium Approximation (EMA). The software indeed allows describing each layer as composed of a mixture of two different materials with optical constants calculated on the basis of EMA method. The porosity can be therefore modelled by considering the layer as composed by a mixture of material and voids (air) in a given percentage.

To simulate the optical behaviour of MoS_2 samples (Fig. 11) we considered an optical model with a single MoS_2 layer on a borosilicate glass substrate, which was previously characterized (as a bare bulk substrate) in order to get its optical constants, whereas for the MoS_2 we used the complex refractive indexes already derived in a previous study ([21], case study #5).

Because of the high defect concentration and the high sulphur deficit detected in the as-deposited MoS_2films, for these studies it was found more reasonable to consider the transmittance and reflectance spectra of the samples after the sulfurization treatments (orange curve in Fig. 11), which (based on optical, XRD and XPS analysis) were found to exhibit physical properties more similar to those expected for a MoS_2thin film.

All the simulation attempts made considering compact MoS_2films (with the measured thickness) were not able to reproduce the experimental spectra, since the predicted transmittance curve was always significantly lower compared to the measured one. Quite good simulations were only obtained by introducing a film porosity, by considering the films as a mixture of MoS_2 and air, whose fraction (f) was refined with the fit.

Table A1 reports the model used for each MoS_2 film (thickness and roughness) and the air fraction (i.e. the porosity) found in each material, revealing an increasing trend of the porosity with the increase of the deposition pressure, in accordance with the results of weight measurements described in the paper.

The experimental spectra and the curves predicted by the used model are shown in Fig. A1 as black dots and blue lines, respectively.

Table A1
Film model (thickness and roughness) and simulated air fraction of MoS_2:Nb films deposited at different pressures.

sample / deposition pressure	film model	air fraction
MoS_2 @ 1 Pa	260 nm rough 15 nm	$f = 20$ %
MoS_2 @ 0.5 Pa	190 nm rough 0 nm	$f = 10$ %
MoS_2 @ 0.11 Pa	190 nm rough 0 nm	$f = 0$ %

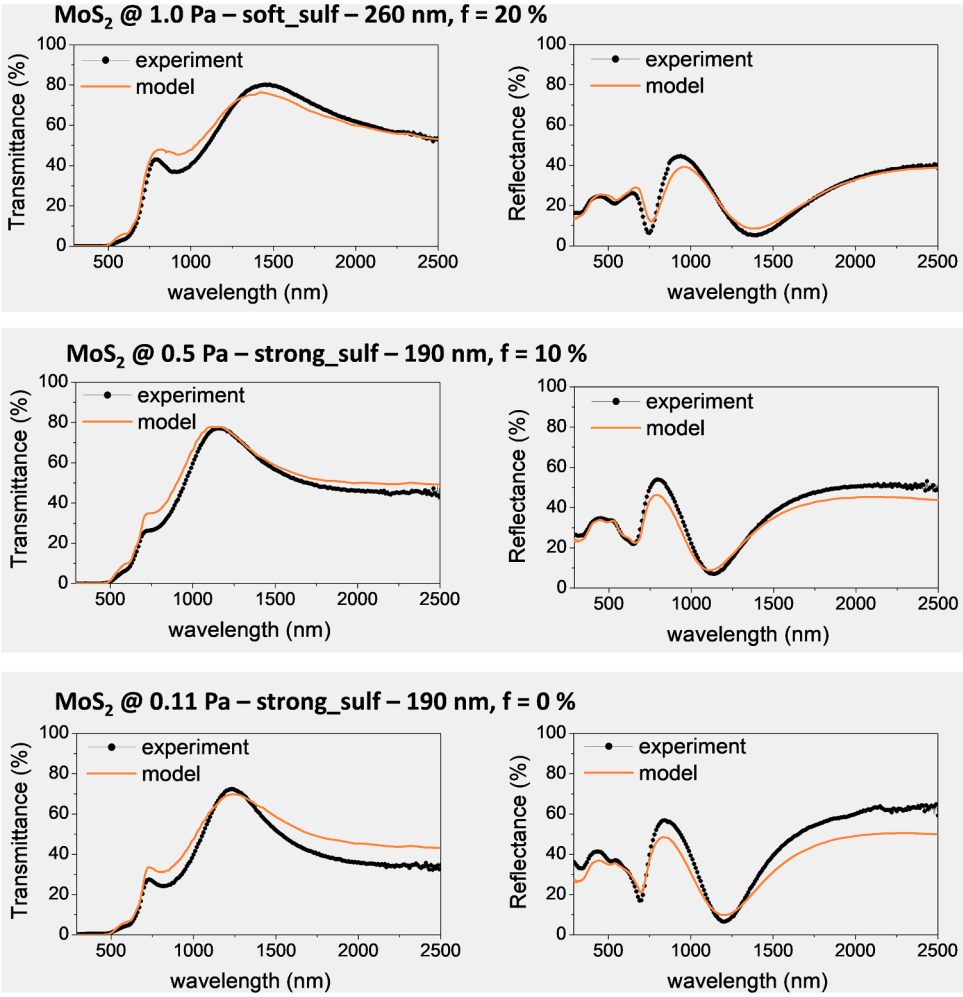

Fig. A1. Optical simulations of Transmittance (Tn) and reflectance (Rn) spectra of three MoS_2 films deposited at different sputtering pressure with the software KSEMAW, including the film porosity (f) in the model.

Appendix B. Additional XPS results

Fig. B1 shows a comparison of Mo3d XPS spectra measured in two as-deposited MoS_2:Nb films, grown with a sputtering pressure of 1 and 0.5 Pa, respectively. The results confirm the presence of metallic Mo (peaked at lower binding energies – doublet at 228–231 eV) in samples produced at the lower pressure of 0.5 Pa. The metallic Mo peak is not detected in films deposited at 1 Pa, which present only the doublet of Mo bonded to sulfur in MoS_2 (228.9–232 eV).

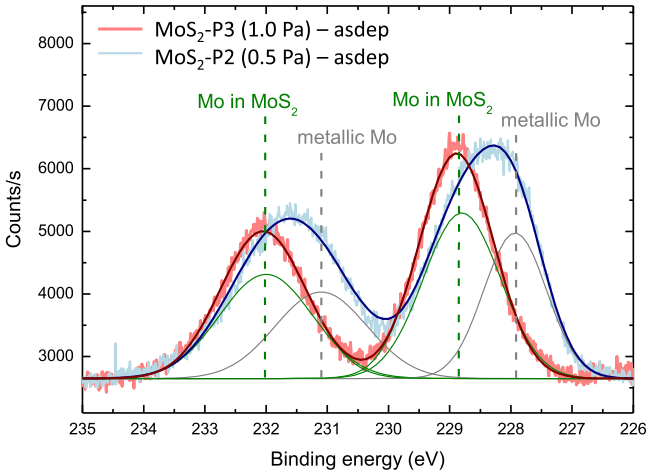

Fig. B1. Mo3d XPS spectra of as-dep MoS_2:Nb films deposited at 1 Pa (light-red plot) and 0.5 Pa (light-blue plot). The bands from metallic Mo and Mo bonded in MoS_2 are represented as thin lines. The dark-red and dark-blue curves are the cumulative fitting of the experimental data.

Fig. B2 reports the normalized XPS spectra of a MoS_2 sample measured as-deposited and after the soft and the strong sulfurization treatments.

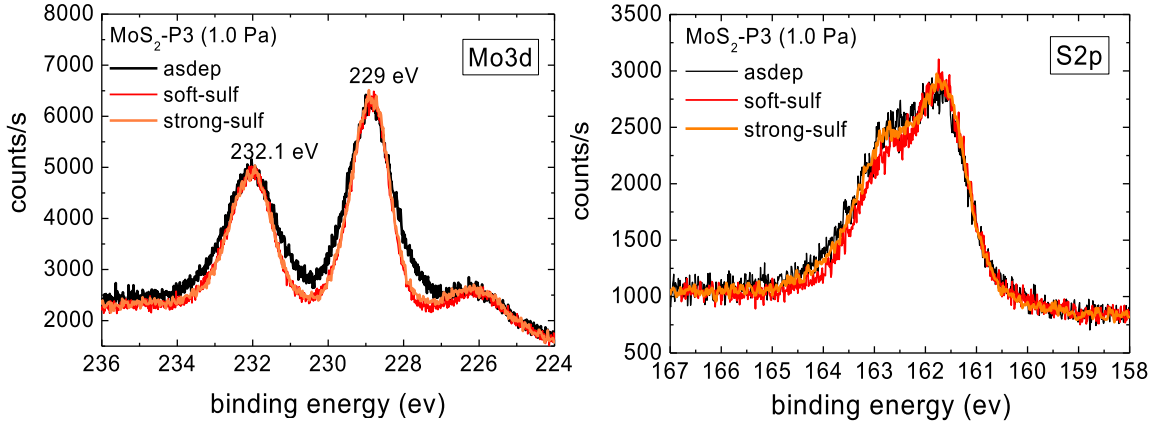

Fig. B2. Normalized XPS spectra of a MoS_2:Nb film measured as deposited and after the *soft* and the *strong* sulfurization treatments.

Appendix C. Optical characterization of the trilayer contacts and of the CZTS/trilayer stack

Fig. C1 reports the absorptance spectra of three MoS_2/FTO/IWO/glass trilayer stacks, with different thicknesses of the MoS_2 film (300 nm, 100 nm, 30 nm) deposited at 1 Pa. Since the CZTS growth process includes a sulfurization treatment at 580 °C, it was quite likely that the final MoS_2 layers located under the CZTS could show properties similar to those of the sulfurized sample. Therefore, each sample was subjected to a *soft-sulf* treatment. The absorptance of both as-deposited and sulfurized samples are shown in the figure. An absorptance as low as 5 % in the 750–1200 nm range can be seen for the thinner (30 nm) sample after the sulfurization (picture in the inset), which was chosen for the device fabrication.

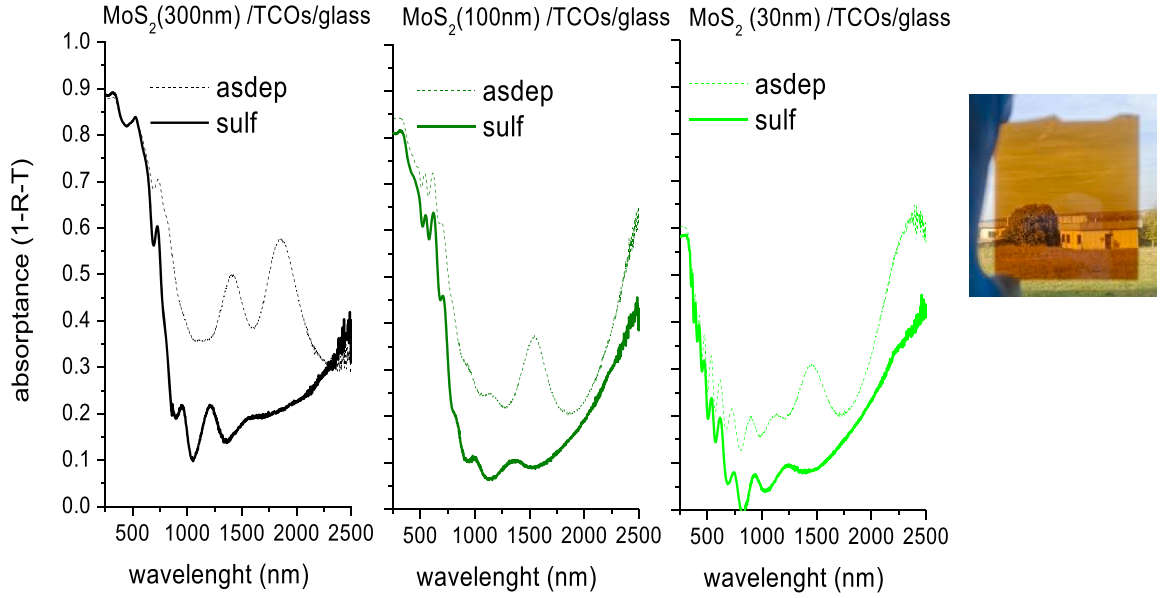

Fig. C1. Absorptance of three MoS_2:Nb/FTO/IWO stacks on BSG, all with MoS_2:Nb deposited at 1 Pa with different thicknesses: 300 nm, 100 nm, 30 nm. For each sample, the as-dep spectrum is compared with the one measured after the soft-sulfurization treatment.

Fig. C2 reports an example of the optical analysis made after the CZTS growth. The graph reports the transmittance T, the reflectance R and the sum of the two spectra for a CZTS/MoS_2:Nb(30 nm)/FTO/IWO/BSG stack in the case of a MoS_2:Nb film deposited at 0.5 Pa. Similar results were obtained using a 30 nm-thick MoS_2:Nb layer deposited at 1 Pa and 0.11 Pa.

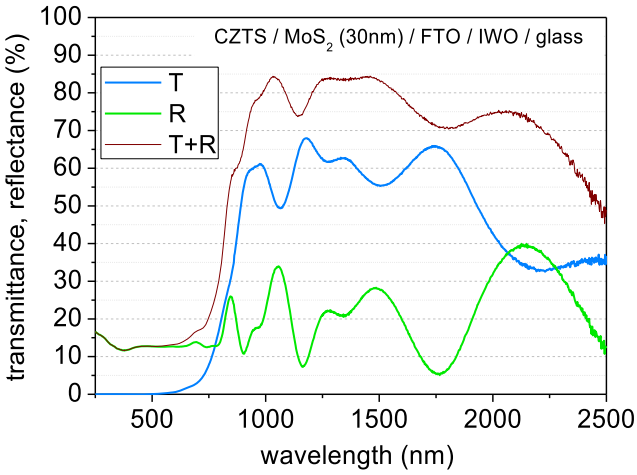

Fig. C2. Transmittance, Reflectance and their sum ($T + R$) spectra of a CZTS/MoS_2:Nb/FTO/IWO/BSG stack, with a 30 nm-thick MoS_2:Nb layer deposited at 0.5 Pa.

References

[1] W. Kautek, H. Gerischer, H. Tributsch, The role of carrier diffusion and indirect optical transitions in the photoelectrochemical behavior of layer type D-Band semiconductors, J. Electrochem. Soc. 127 (11) (1980) 2471–2478, https://doi.org/10.1149/1.2129499.

[2] K.K. Kam, B.A. Parkinson, Detailed photocurrent spectroscopy of the semiconducting group VI transition metal dichalcogenides, J. Phys. Chem. 86 (1982) 463–467.

[3] J.A. Wilson, A.D. Yoffe, The transition metal dichalcogenides discussion and interpretation of the observed optical, electrical and structural properties, Adv. Phys. 18 (1969) 193–335, https://doi.org/10.1080/00018736900101307.

[4] T. Shimada, F.S. Ohuchi, B.A. Parkinson, Work function and photothreshold of layered metal dichalcogenides, Jap. J. Appl. Phys. 33 (1994) 2696–2698, https://doi.org/10.1143/JJAP.33.2696.

[5] H. Qiu, T. Xu, Z. Wang, W. Ren, H. Nan, Z. Ni, Q. Chen, S. Yuan, F. Miao, F. Song, G. Long, Y. Shi, L. Sun, J. Wang, X. Wan, Hopping transport through defect-induced localized states in molybdenum disulphide, Nat. Comm. 4 (2013) 2642, https://doi.org/10.1038/ncomms3642.

[6] T. Horiguchi, T. Hamada, M. Hamada, I. Muneta, K. Kakushima, K. Tsutsui, T. Tatsumi, S. Tomiya, H. Wakabayashi, Positive Seebeck coefficient of niobium-doped MoS_2 film deposited by sputtering and activated by sulfur vapor annealing, Jpn. J. Appl. Phys. 61 (2022) 075506, https://doi.org/10.35848/1347-4065/ac7621.

[7] K. Matsuura, T. Ohashi, I. Muneta, S. Ishihara, K. Kakushima, K. Tsutsui, A. Ogura, H. Wakabayashi, Low-carrier-density sputtered MoS_2 film by vapor-phase sulfurization, J. Electr. Mater. 47 (2018) 3497, https://doi.org/10.1007/s11664-018-6191-z.

[8] H. Komsa, A.V. Krasheninnikov, Native defects in bulk and monolayer MoS_2 from first principles, Phys. Rev. B 91 (2015) 125304, https://doi.org/10.1103/PhysRevB.91.125304.

[9] K. Dolui, I. Rungger, C.D. Pemmaraju, S. Sanvito, Possible doping strategies for MoS_2 monolayers: an ab initio study, Phys. Rev. B 88 (2013) 75420, https://doi.org/10.1103/PhysRevB.88.075420.

[10] R. Friend, A. Yoffe, Electronic properties of intercalation complexes of the transition metal dichalcogenides, Adv. Phys. 36 (1987) 1–94, https://doi.org/10.1080/00018738700101951.

[11] A. Molle, F. Fabbri, D. Campi, A. Lamperti, E. Rotunno, E. Cinquanta, L. Lazzarini, D. Kaplan, V. Swaminathan, M. Bernasconi, M. Longo, G. Salviati, Evidence of native Cs impurities and metal-insulator transition in MoS_2 natural crystals, Adv. Electr. Mater. 2 (2016) 1600091, https://doi.org/10.1002/aelm.201600091.

[12] M. Chen, H. Nam, S. Wi, L. Ji, X. Ren, L. Bian, S. Lu, X. Liang, Stable few-layer MoS_2 rectifying diodes formed by plasma-assisted doping, Appl. Phys. Lett. 103 (2013) 142110, https://doi.org/10.1063/1.4824205.

[13] A.T. Neal, R. Pachter, S. Mou, P-type conduction in two-dimensional MoS_2 via oxygen incorporation, Appl. Phys. Lett. 110 (2017) 193103, https://doi.org/10.1063/1.4983092.

[14] E. Xu, H. Liu, K. Park, Z. Li, Y. Losovyj, M. Starr, M. Werbianskyj, H. Fertig, S. Zhang, P-Type transition-metal doping of large-area MoS_2 thin films grown by chemical vapor deposition, Nanoscale 9 (2017) 3576–3584, https://doi.org/10.1039/c6nr09495c.

[15] A. Nipane, D. Karmakar, N. Kaushik, N. Karande, S. Lodha, Few-layer MoS_2 p-type devices enabled by selective doping using low energy phosphorus implantation, ACS Nano 10 (2016) 2128–2137, https://doi.org/10.1021/acsnano.5b06529.

[16] J. Suh, T. Park, D. Lin, D. Fu, J. Park, H. Jung, Y. Chen, C. Ko, C. Jang, Y. Sun, R. Sinclair, J. Chang, S. Tongay, J. Wu, Doping against the native propensity of MoS_2: degenerate hole doping by cation substitution, Nano Lett. 14 (2014) 6976–6982.

[17] II M. Laskar, D. Nath, L. Ma, E. Lee, C. Lee, T. Kent, Z. Yang, R. Mishra, M. Roldan, J.-C. Idrobo, S. Pantelides, S. Pennycook, R. Myers, Y. Wu, S. Rajan, P-type doping of MoS_2 thin films using Nb, Appl. Phys. Lett. 104 (2014) 092104, https://doi.org/10.1063/1.4867197.

[18] M. Valentini, C. Malerba, L. Serenelli, M. Izzi, E. Salza, M. Tucci, A. Mittiga, Fabrication of monolithic CZTS/Si tandem cells by development of the intermediate connection, Solar Energy 190 (2019) 414–419, https://doi.org/10.1016/j.solener.2019.08.029.

[19] S. Kim, J. Lim, R. Sahu, O. Kasian, L.-T. Stephenson, C. Scheu, B. Gault, Direct imaging of dopant and impurity distributions in 2D MoS_2, Adv. Mater. 32 (2020) 1907235, https://doi.org/10.1002/adma.201907235.

[20] T. Komesu, D. Le, X. Zhang, Q. Ma, E. Schwier, Y. Kojima, M. Zheng, H. Iwasawa, K. Shimada, M. Taniguchi, L. Bartels, T. Rahman, P. Dowben, Occupied and unoccupied electronic structure of Na doped MoS_2(0001), Appl. Phys. Lett. 105 (2014) 241602, https://doi.org/10.1063/1.4903824.

[21] M. Montecchi, A. Mittiga, C. Malerba, F. Menchini, KSEMAW: an open-source software for the analysis of spectrophotometric, ellipsometric and photothermal deflection spectroscopy measurements-version 2, Open Res. Eur. 1 (2021) 95, https://doi.org/10.12688/openreseurope.13842.1.

[22] C. Malerba, M. Valentini, A. Mittiga, Cation disorder in Cu_2ZnSnS_4 thin films: effect on solar cell performances, Solar RRL 1 (2017) 1700101, https://doi.org/10.1002/solr.201700101.

[23] E. Ojeda-Duran, K. Monfil-Leyva, J. Andrade-Arvizu, I. Becerril-Romero, Y. Sanchez, R. Fonoll-Rubio, M. Guc, Z. Jehl, J. Luna-Lopez, A. Munoz-Zurita, J. Hernandez-de la Luz, V. Izquierdo-Roca, M. Placidi, E. Saucedo, CZTS solar cells and the possibility of increasing V_{OC} using evaporated Al_2O_3 at the CZTS/CdS interface, Solar Energy 198 (2020) 696–703, https://doi.org/10.1016/j.solener.2020.02.009.

[24] E. Ojeda-Duran, K. Monfil-Leyva, J. Andrade-Arvizu, I. Becerril-Romero, Y. Sanchez, R. Fonoll-Rubio, M. Guc, Z. Li-Kao, J. Luna-Lopez, E. Saucedo, High efficiency Cu_2ZnSnS_4 solar cells over FTO substrates and their CZTS/CdS interface passivation via thermal evaporation of Al_2O_3, J. Mater. Chem. C 9 (2021) 5356–5361, https://doi.org/10.1039/d1tc00880c.

[25] C. Andres, T. Schwarz, S. Haass, T. Weiss, R. Carron, R. Caballero, R. Figi, C. Schreiner, M. Bürki, A. Tiwari, Y. Romanyuk, Decoupling of optoelectronic properties from morphological changes in sodium treated kesterite thin film solar cells, Solar Energy 175 (2018) 94–100, https://doi.org/10.1016/j.solener.2018.03.067.

[26] K. Rasamani, K. Alimohammadi, Y. Sun, Interlayer-expanded MoS_2, Mater. Today 20 (2017) 83–91, https://doi.org/10.1016/j.mattod.2016.10.004.

[27] B.C. Kaindl, R. and. Bayer, R. Resel, T. Muller, V. Skakalova, G. Habler, R. Abart, A. Cherevan, D. Eder, M. Blatter, F. Fischer, J. Meyer, D. Polyushkin, W. Waldhauser, Growth, structure and stability of sputter-deposited *MoS_2* thin films, Beilstein J. Nanotechnol. 8 (2017) 1115–1126, https://doi.org/10.3762/bjnano.8.113.

[28] Z. Lei, J. Zhan, L. Tang, Y. Zhang, Y. Wang, Recent development of metallic (1T) phase of molybdenum disulfide for energy conversion and storage, Adv. Energy Mater. 8 (2018) 1703482, https://doi.org/10.1002/aenm.201703482.

[29] Z. Wu, D. Wang, A. Sun, Surfactant-assisted fabrication of MoS_2 nanospheres, J. Mater. Sci. 45 (2010) 182–187, https://doi.org/10.1007/s10853-009-3914-9, 45, 182 –187 (2010).

[30] M. Wu, J. Zhan, K. Wu, Z. Li, L. Wang, B. Geng, L. Wang, D. Pan, Metallic 1T MoS_2 nanosheet arrays vertically grown on activated carbon fiber cloth for enhanced Li-ion storage performance, J Mater. Chem. A 5 (2017) 14061–14069, https://doi.org/10.1039/c7ta03497k.

[31] X. Wang, X. Shen, Z. Wang, R. Yu, L. Chen, Atomic-scale clarification of structural transition of MoS_2 upon sodium intercalation, ACS Nano 8 (2014) 11394–11400, https://doi.org/10.1021/nn505501v.
[32] B.C. Bayer, R. Kaindl, M.R.A. Monazam, T. Susi, J. Kotakoski, T. Gupta, W. Eder, D. Waldhauser, J. Meyer, Atomic-scale in situ observations of crystallization and restructuring processes in two-dimensional MoS_2 films, ACS Nano 12 (2018) 8758–8769, https://doi.org/10.1021/acsnano.8b04945.
[33] editorW.M. H (Ed.), CRC Handbook of Chemistry and Physics, 95th ed, CRC Press/Taylor and Francis, Boca Raton, FL, 2014, 90th edition.
[34] F. Vullers, R. Spolenak, Alpha- vs. beta-W nanocrystalline thin films: a comprehensive study of sputter parameters and resulting materials' properties, Thin Solid Films 577 (2015) 26–34, https://doi.org/10.1016/j.tsf.2015.01.030.
[35] C. Malerba, M. Valentini, C. Azanza Ricardo, A. Rinaldi, E. Cappelletto, P. Scardi, A. Mittiga, Blistering in Cu_2ZnSnS_4 thin films: correlation with residual stresses, Mater. Des. 108 (2016) 725–735, https://doi.org/10.1016/j.matdes.2016.07.019.
[36] M. Montecchi, A. Mittiga, C. Malerba, F. Menchini, KSEMAW: an open source software for the analysis of spectrophotometric, ellipsometric and photothermal deflection spectroscopy measurements, Open Res. Eur. 1 (2021) 95, https://doi.org/10.12688/openreseurope.13842.1.
[37] R. Bichsel, P. Buffat, F. Levy, Correlation between process conditions, chemical composition and morphology of MoS_2 films prepared by RF planar magnetron sputtering, J. Phys. D: Appl. Phys. 19 (1986) 1575, https://doi.org/10.1088/0022-3727/19/8/025. -158 19, 1575 –1585 (1986).
[38] P. Afanasiev, Synthetic approaches to the molybdenum sulfide materials, C. R. Chim. 11 (2008) 159–182, https://doi.org/10.1016/j.crci.2007.04.009.
[39] J. Wildervanck, F. Jellinek, Preparation and crystallinity of molybdenum and tungsten sulfides, ZAAC - J. Inorg. Gen. Chem. 328 (1964) 309–318, https://doi.org/10.1002/zaac.19643280514.
[40] D. Merki, S. Fierro, H. Vrubel, X. Hu, Amorphous molybdenum sulfide films as catalysts for electrochemical hydrogen production in water, Chem. Sci. 2 (2011) 1262, https://doi.org/10.1039/c1sc00117e.
[41] T. Weber, J.C. Muijsers, J.W. Niemantsverdriet, Structure of amorphous MoS_3, J. Phys. Chem. 99 (1995) 9194–9200, https://doi.org/10.1021/j100022a037.
[42] J. Kibsgaard, T. Jaramillo, F. Besenbacher, Building an appropriate active-site motif into a hydrogen-evolution catalyst with thiomolybdate $[Mo_3S_{13}]^{2-}$ clusters, Nat. Chem. 6 (2014) 248, https://doi.org/10.1038/NCHEM.1853.
[43] S.J. Lee, Y. Son, J. Choi, S. Kim, S.S. Park, Morphology and catalytic performance of MoS_2 hydrothermally synthesized at various pH values, Catalysts 11 (2021) 1229, https://doi.org/10.3390/catal11101229.
[44] P. Cheng, K. Sun, Y. Hu, Memristive behavior and ideal memristor of 1T phase MoS_2 nanosheets, Nano Lett. 16 (2016) 572, https://doi.org/10.1021/acs.nanolett.5b04260.
[45] H. Wang, P. Skeldon, G. Thompson, XPS studies of MoS_2 formation from ammonium tetrathiomolybdate solutions, Surf. Coat. Tech. 91 (1997) 200–207, https://doi.org/10.1016/S0257-8972(96)03186-6.
[46] P. Panigrahi, A. Pathak, Aqueous medium synthesis route for randomly stacked molybdenum disulfide, J. Nanoparticles 2013 (2013) 671214, https://doi.org/10.1155/2013/671214.
[47] R. Kappera, D. Voiry, S.E. Yalcin, B. Branch, G. Gupta, A. Mohite, M. Chhowalla, Phase-engineered low-resistance contacts for ultrathin MoS_2 transistors, Nat. Mater. 13 (2014) 1128–1134, https://doi.org/10.1038/nmat4080.
[48] X. Liu, Q. Li, Q. He, A. Khalil, D. Liu, T. Xiang, X. Wu, L. Song, Gram-scale aqueous synthesis of stable few-layered 1T-MoS_2 : applications for visible-light-driven photocatalytic hydrogen evolution, Small 11 (2015) 5556–5564, https://doi.org/10.1002/smll.201501822.
[49] C. Wagner, J. Taylor, Contributions to screening in the solid state by electron systems of remote atoms: effects to photoelectron and Auger transitions, J. Electr. Spectros. Relat. Phenomena 28 (1982) 211–217, https://doi.org/10.1016/0368-2048(82)85044-5.
[50] A. Santoni, F. Rondino, C. Malerba, M. Valentini, A. Mittiga, Electronic structure of Ar^+ ion-sputtered thin-Film MoS_2: a XPS and IPES study, Appl. Surf. Sci. 392 (2017) 795–800, https://doi.org/10.1016/j.apsusc.2016.09.007.
[51] S. McDonnell, R. Addou, C. Buie, R.M. Wallace, C. Hinkle, Defect-dominated doping and contact resistance in MoS_2, ACS Nano 8 (2014) 2880–2888, https://doi.org/10.1021/nn500044q.
[52] S. Hsieh, W. Chen, K. Ohdaira, Barrier performance of ITO film on textured Si substrate, J. Mater. Sci.: Mater. Electr. 31 (2020) 13808–13816, https://doi.org/10.1007/s10854-020-03941-3.
[53] S. Hu, K. Lu, H. Ning, Z. Fang, X. Liu, W. Xie, R. Yao, J. Zou, M. Xu, J. Peng, Effect of ITO serving as a barrier layer for Cu electrodes on performance of a-IGZO TFT, IEEE Electr. Dev. Lett. 39 (2018) 504–507, https://doi.org/10.1109/LED.2018.2800725.